

Chapter 12

Two-Phase Flow Patterns

(This chapter was updated in 2007)

SUMMARY: For two-phase flows, the respective distribution of the liquid and vapor phases in the flow channel is an important aspect of their description. Their respective distributions take on some commonly observed flow structures, which are defined as two-phase flow patterns that have particular identifying characteristics. Heat transfer coefficients and pressure drops are closely related to the local two-phase flow structure of the fluid, and thus two-phase flow pattern prediction is an important aspect of modeling evaporation and condensation. In fact, recent heat transfer models for predicting intube boiling and condensation are based on the local flow pattern and hence, by necessity, require reliable flow pattern maps to identify what type of flow pattern exists at the local flow conditions. Analogous to predicting the transition from laminar to turbulent flow in single-phase flows, two-phase flow pattern maps are used for predicting the transition from one type of two-phase flow pattern to another.

In this chapter, first the geometric characteristics of flow patterns inside tubes will be described for vertical upward and horizontal flows. Next, several of the widely quoted, older flow pattern maps for vertical and horizontal flows will be presented. Then, a recent flow pattern map and its flow regime transition equations specifically for adiabatic flows and in particular for evaporation and condensation in horizontal tubes will be presented. Finally, flow patterns in two-phase flows over tube bundles will be addressed and a flow pattern map proposed for those flows will be shown.

12.1 Flow Patterns in Vertical Tubes

For co-current upflow of gas and liquid in a vertical tube, the liquid and gas phases distribute themselves into several recognizable flow structures. These are referred to as flow patterns and they are depicted in Figure 12.1 and can be described as follows:

- **Bubbly flow.** Numerous bubbles are observable as the gas is dispersed in the form of discrete bubbles in the continuous liquid phase. The bubbles may vary widely in size and shape but they are typically nearly spherical and are much smaller than the diameter of the tube itself.
- **Slug flow.** With increasing gas void fraction, the proximity of the bubbles is very close such that bubbles collide and coalesce to form larger bubbles, which are similar in dimension to the tube diameter. These bubbles have a characteristic shape similar to a bullet with a hemispherical nose with a blunt tail end. They are commonly referred to as Taylor bubbles after the instability of that name. Taylor bubbles are separated from one another by slugs of liquid, which may include small bubbles. Taylor bubbles are surrounded by a thin liquid film between them and the tube wall, which may flow downward due to the force of gravity, even though the net flow of fluid is upward.
- **Churn flow.** Increasing the velocity of the flow, the structure of the flow becomes unstable with the fluid traveling up and down in an oscillatory fashion but with a net upward flow. The instability is the result of the relative parity of the gravity and shear forces acting in opposing directions on the thin film of liquid of Taylor bubbles. This flow pattern is in fact an intermediate regime between the slug flow and annular flow regimes. In small diameter tubes, churn flow may not develop at all and the flow passes directly from slug flow to annular flow. Churn flow is typically a flow regime to be

avoided in two-phase transfer lines, such as those from a reboiler back to a distillation column or in refrigerant piping networks, because the mass of the slugs may have a destructive consequence on the piping system.

- **Annular flow.** Once the interfacial shear of the high velocity gas on the liquid film becomes dominant over gravity, the liquid is expelled from the center of the tube and flows as a thin film on the wall (forming an annular ring of liquid) while the gas flows as a continuous phase up the center of the tube. The interface is disturbed by high frequency waves and ripples. In addition, liquid may be entrained in the gas core as small droplets, so much so that the fraction of liquid entrained may become similar to that in the film. This flow regime is particularly stable and is the desired flow pattern for two-phase pipe flows.
- **Wispy annular flow.** When the flow rate is further increased, the entrained droplets may form transient coherent structures as clouds or wisps of liquid in the central vapor core.
- **Mist flow.** At very high gas flow rates, the annular film is thinned by the shear of the gas core on the interface until it becomes unstable and is destroyed, such that all the liquid is entrained as droplets in the continuous gas phase, analogous to the inverse of the bubbly flow regime. Impinging liquid droplets intermittently wet the tube wall locally. The droplets in the mist are often too small to be seen without special lighting and/or magnification.

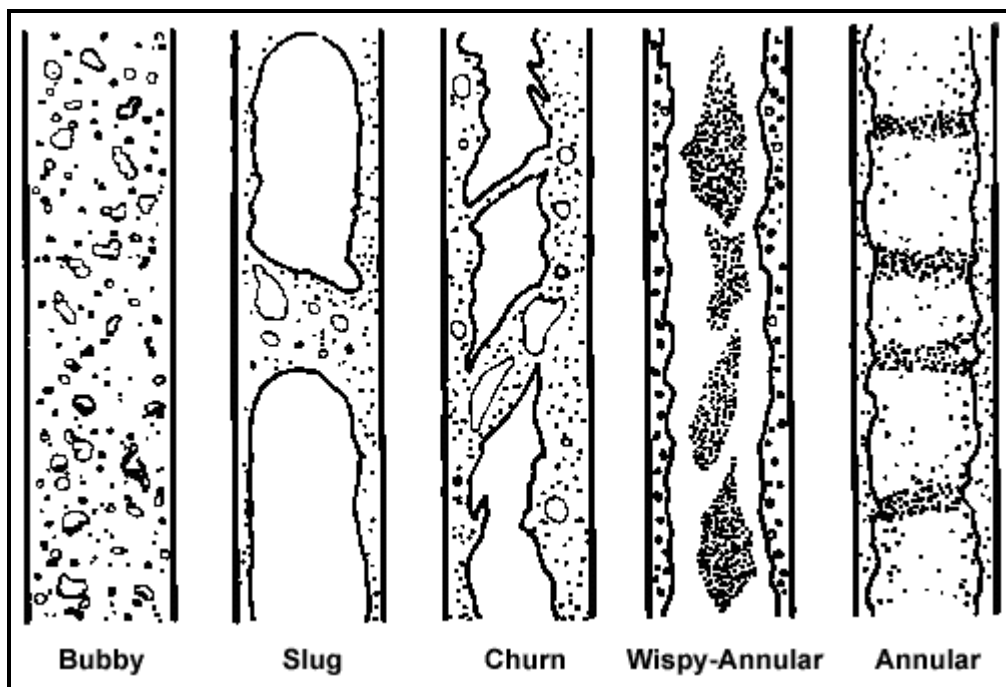


Figure 12.1. Two-phase flow patterns in vertical upflow.

12.2 Flow Patterns in Horizontal Tubes

Two-phase flow patterns in horizontal tubes are similar to those in vertical flows but the distribution of the liquid is influenced by gravity that acts to stratify the liquid to the bottom of the tube and the gas to the top. Flow patterns for co-current flow of gas and liquid in a horizontal tube are shown in Figure 12.2 and are categorized as follows:

- **Bubbly flow.** The gas bubbles are dispersed in the liquid with a high concentration of bubbles in the upper half of the tube due to their buoyancy. When shear forces are dominant, the bubbles tend to disperse uniformly in the tube. In horizontal flows, the regime typically only occurs at high mass flow rates.
- **Stratified flow.** At low liquid and gas velocities, complete separation of the two phases occurs. The gas goes to the top and the liquid to the bottom of the tube, separated by an undisturbed horizontal interface. Hence the liquid and gas are fully stratified in this regime.
- **Stratified-wavy flow.** Increasing the gas velocity in a stratified flow, waves are formed on the interface and travel in the direction of flow. The amplitude of the waves is notable and depends on the relative velocity of the two phases; however, their crests do not reach the top of the tube. The waves climb up the sides of the tube, leaving thin films of liquid on the wall after the passage of the wave.
- **Intermittent flow.** Further increasing the gas velocity, these interfacial waves become large enough to wash the top of the tube. This regime is characterized by large amplitude waves intermittently washing the top of the tube with smaller amplitude waves in between. Large amplitude waves often contain entrained bubbles. The top wall is nearly continuously wetted by the large amplitude waves and the thin liquid films left behind. Intermittent flow is also a composite of the plug and slug flow regimes. These subcategories are characterized as follows:
 - **Plug flow.** This flow regime has liquid plugs that are separated by elongated gas bubbles. The diameters of the elongated bubbles are smaller than the tube such that the liquid phase is continuous along the bottom of the tube below the elongated bubbles. Plug flow is also sometimes referred to as *elongated bubble flow*.
 - **Slug flow.** At higher gas velocities, the diameters of elongated bubbles become similar in size to the channel height. The liquid slugs separating such elongated bubbles can also be described as large amplitude waves.
- **Annular flow.** At even larger gas flow rates, the liquid forms a continuous annular film around the perimeter of the tube, similar to that in vertical flow but the liquid film is thicker at the bottom than the top. The interface between the liquid annulus and the vapor core is disturbed by small amplitude waves and droplets may be dispersed in the gas core. At high gas fractions, the top of the tube with its thinner film becomes dry first, so that the annular film covers only part of the tube perimeter and thus this is then classified as stratified-wavy flow.
- **Mist flow.** Similar to vertical flow, at very high gas velocities, all the liquid may be stripped from the wall and entrained as small droplets in the now continuous gas phase.

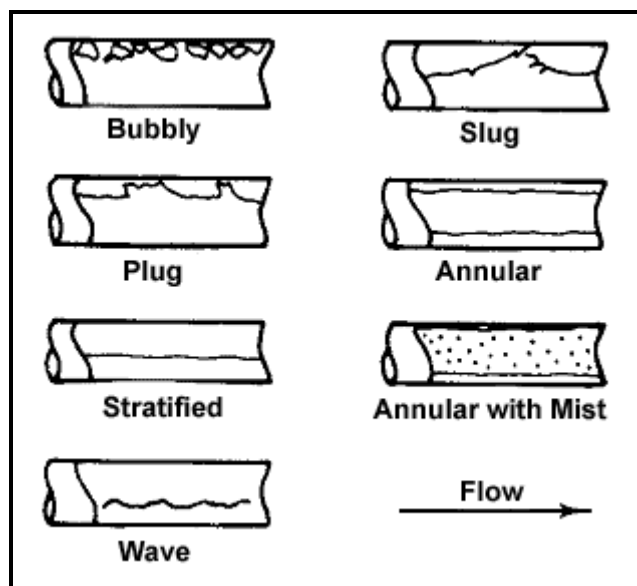


Figure 12.2. Two-phase flow patterns in horizontal flow.

12.3 Older Adiabatic Flow Pattern Maps for Vertical and Horizontal Flows in Tubes

For vertical upflow, Figure 12.3 shows the typical order of the flow regimes that would be encountered from inlet to outlet of an evaporator tube. The flow pattern typically begins in the bubbly flow regime at the inlet at the onset of nucleate boiling in the tube. This onset of nucleate boiling may begin in the subcooled zone of the tube, where bubbles nucleate in the superheated thermal boundary layer on the heated tube wall but tend to condense in the subcooled core. The onset of nucleate boiling may also be delayed to local vapor qualities greater than zero in the case of a subcooled inlet and a low heat flux. After bubbly flow the slug flow regime is entered and then the annular flow regime with its characteristic annular film of liquid. This film eventually dries out or the film is entrained by the interfacial vapor shear, taking the flow into the mist flow regime. The entrained liquid droplets may persist in the flow past the point of the vapor quality equal to 1.0.

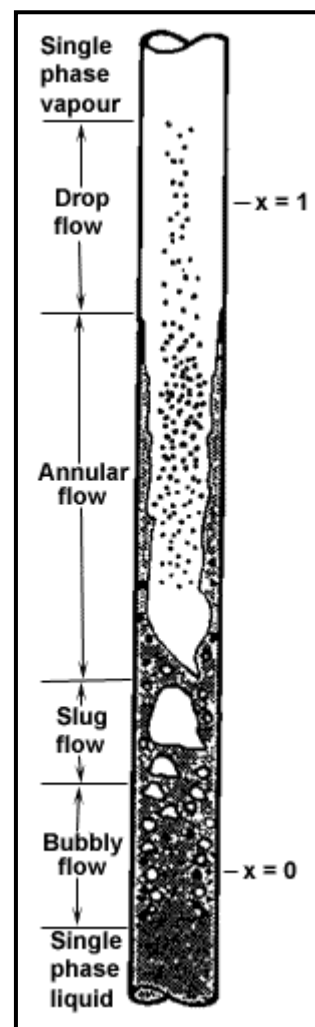


Figure 12.3. Flow regimes in a vertical evaporator tube from Collier and Thome (1994).

To predict the local flow pattern in a tube, a flow pattern map is used. It is a diagram that displays the transition boundaries between the flow patterns and is typically plotted on log-log axes using dimensionless parameters to represent the liquid and gas velocities. Fair (1960) and Hewitt and Roberts (1969) proposed widely quoted flow pattern maps for vertical upflow, illustrated in Figures 12.4 and 12.5, respectively. The most widely quoted flow pattern maps for predicting the transition between two-phase flow regimes for adiabatic flow in horizontal tubes are those of Baker (1954) and Taitel and Dukler (1976), depicted in Figures 12.6 and 12.7. Transition curves on flow pattern maps should be considered as transition zones analogous to that between laminar and turbulent flows. For a more comprehensive and fundamental treatment of two-phase flow transitions, refer to Barnea and Taitel (1986).

To utilize the Fair (1960) map illustrated in Figure 12.4, first one must calculate the value of the x-axis and the mass velocity (here in lb/h ft^2) for the particular application at hand. The two values are then used to read vertically up and horizontally across the graph to find the point of intersection. The location of this point thus identifies where the flow is in the bubbly flow, slug flow, annular flow or mist flow regime, where the dark lines show the transition thresholds between the regimes.

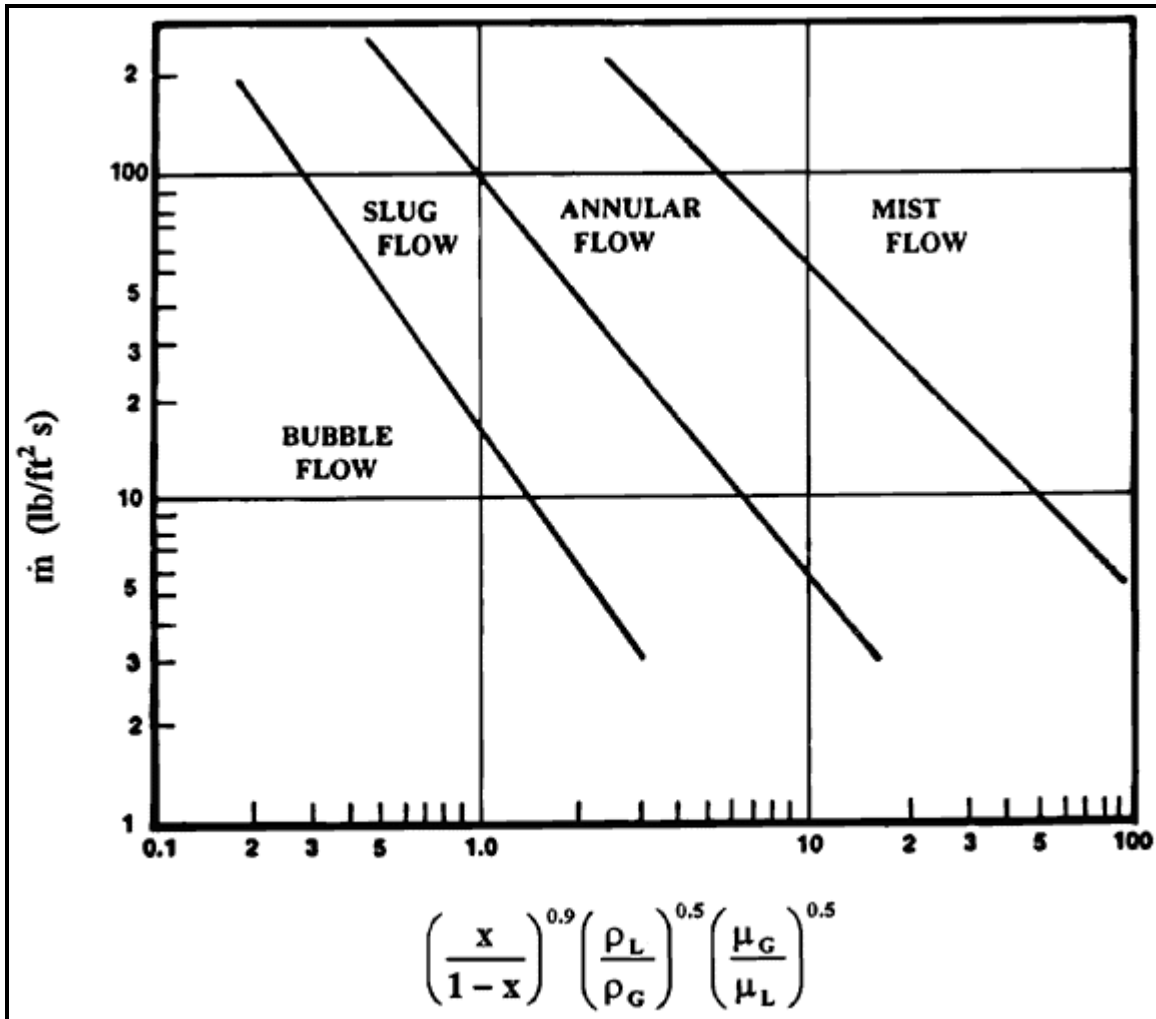


Figure 12.4. Two-phase flow pattern map of Fair (1960) for vertical tubes.

To use the Hewitt and Roberts (1969) map for vertical up flow shown in Figure 12.5, the mass velocities of the liquid \dot{m}_L and gas (or vapor) \dot{m}_G must first be calculated using the local vapor quality. Then the values of the x and y coordinates are determined and the intersection of these two values on the map identifies the flow pattern predicted to exist at these flow conditions.

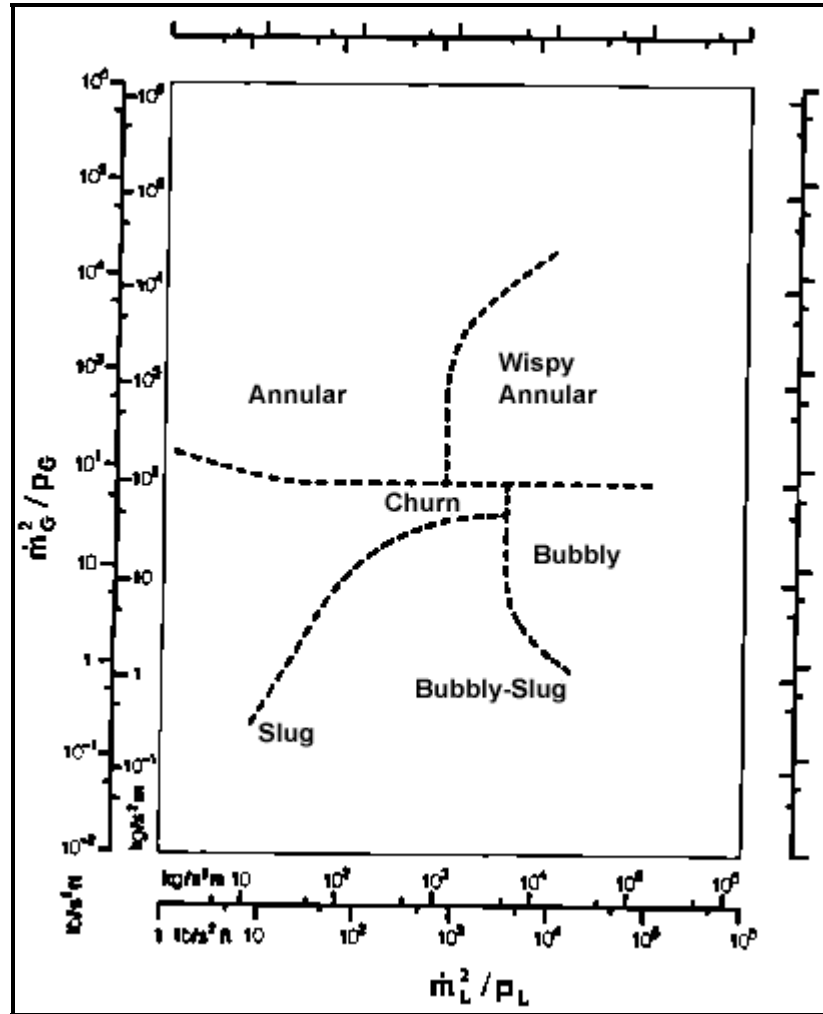


Figure 12.5. Two-phase flow pattern map of Hewitt and Roberts (1969) for vertical tubes.

The Baker (1954) map for horizontal two-phase flow in tubes shown in Figure 12.6 is presented in both SI and English units. To utilize the map, first the mass velocities of the liquid and vapor must be determined. Then his parameters λ and ψ are calculated. The gas-phase parameter λ is:

$$\lambda = \left(\frac{\rho_G}{\rho_{air}} \frac{\rho_L}{\rho_{water}} \right)^{1/2} \quad [12.3.1]$$

and the liquid-phase parameter ψ is:

$$\psi = \left(\frac{\sigma_{water}}{\sigma} \right) \left[\left(\frac{\mu_L}{\mu_{water}} \right) \left(\frac{\rho_{water}}{\rho_L} \right)^2 \right]^{1/3} \quad [12.3.2]$$

where ρ_G , ρ_L , μ_L and σ are properties of the fluid and the reference properties are:

- $\rho_{\text{water}} = 1000 \text{ kg/m}^3$;
- $\rho_{\text{air}} = 1.23 \text{ kg/m}^3$;
- $\mu_{\text{water}} = 0.001 \text{ Ns/m}^2$;
- $\sigma_{\text{water}} = 0.072 \text{ N/m}$.

The values of the x-axis and y-axis are then determined to identify the particular flow regime.

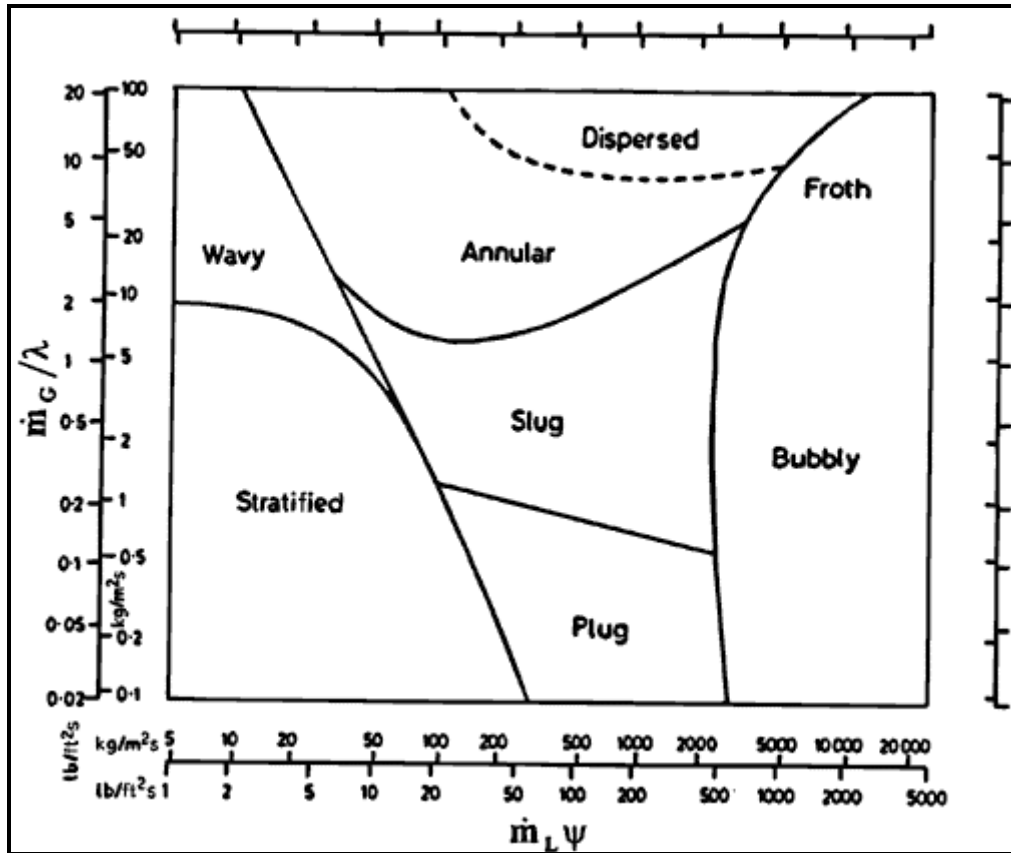


Figure 12.6. Two-phase flow pattern map of Baker (1954) for horizontal tubes.

The Taitel and Dukler (1976) map for horizontal flow in tubes shown in Figure 12.7 is based on their analytical analysis of the flow transition mechanisms together with empirical selection of several parameters. The map uses the Martinelli parameter X , the gas Froude number Fr_G and the parameters T and K and is composed of three graphs. The Martinelli parameter is:

$$X = \left[\frac{(dp/dz)_L}{(dp/dz)_G} \right]^{1/2} \quad [12.3.3]$$

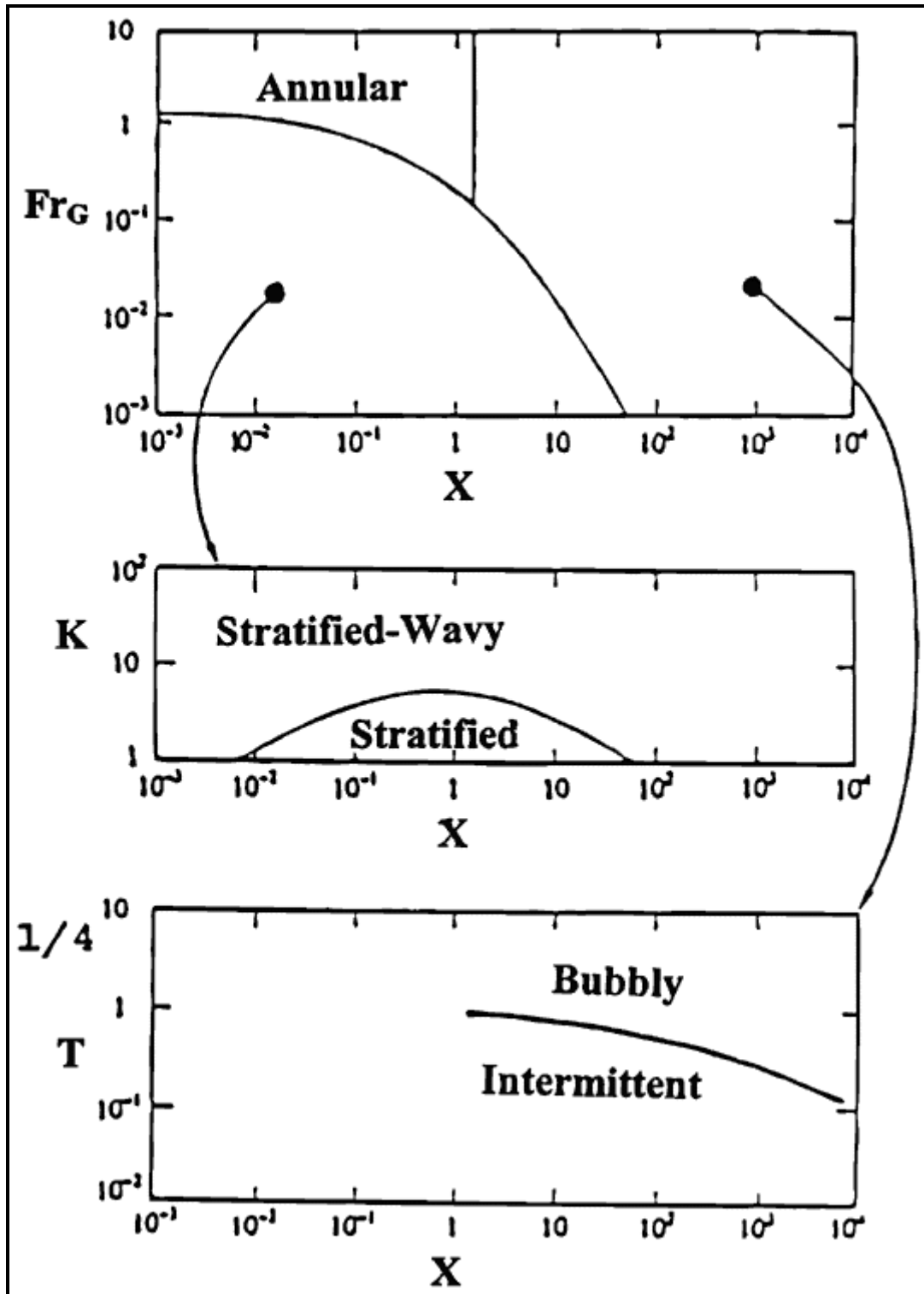


Figure 12.7. Two-phase flow pattern map of Taitel and Dukler (1976) for horizontal tubes.

The gas-phase Froude number is:

$$Fr_G = \frac{\dot{m}_G}{[\rho_G(\rho_L - \rho_G)d_i g]^{1/2}} \quad [12.3.4]$$

Their parameter T is:

$$T = \left[\frac{|(dp/dz)_L|}{g(\rho_L - \rho_G)} \right]^{1/2} \quad [12.3.5]$$

where g is the acceleration due to gravity ($g = 9.81 \text{ m/s}^2$). Their parameter K is:

$$K = Fr_G Re_L^{1/2} \quad [12.3.6]$$

where the liquid-phase and vapor-phase Reynolds numbers are:

$$Re_L = \frac{\dot{m}_L d_i}{\mu_L} \quad [12.3.7]$$

$$Re_G = \frac{\dot{m}_G d_i}{\mu_G} \quad [12.3.8]$$

The pressure gradient of the flow for phase k (where k is either L or G) is:

$$(dp/dz)_k = -\frac{2f_k \dot{m}_k^2}{\rho_k d_i} \quad [12.3.9]$$

For $Re_k < 2000$, the laminar flow friction factor equation is used:

$$f_k = \frac{16}{Re_k} \quad [12.3.10]$$

For $Re_k > 2000$, the turbulent flow friction factor equation is used (even for the transition regime from 2000 to 10,000):

$$f_k = \frac{0.079}{Re_k^{1/4}} \quad [12.3.11]$$

To implement the map, one first determines the Martinelli parameter X and Fr_G . Using these two parameters on the top graph, if their coordinates fall in the annular flow regime, then the flow pattern is annular. If the coordinates of Fr_G and X fall in the lower left zone of the top graph, then K is calculated. Using K and X in the middle graph, the flow regime is identified as either stratified-wavy or as fully stratified. If the coordinates of Fr_G and X fall in the right zone on the top graph, then T is calculated. Using T and X in the bottom graph, the flow regime is identified as either bubbly flow or intermittent (plug or slug) flow.

These flow pattern maps were all developed for adiabatic two-phase flows but are often extrapolated for use with the diabatic processes of evaporation or condensation. As with any extrapolation, this may or may not produce reliable results. For a description of flow pattern transition theory, a good review was presented by Taitel (1990).

12.4 Flow Pattern Map for Evaporation in Horizontal Tubes

For evaporation in horizontal tubes, Figure 12.8 from Collier and Thome (1994) depicts the typical flow regimes, including cross-sectional views of the flow structure. For condensation, the flow regimes are similar with the exception that the top tube wall is not dry in stratified types of flow but instead is coated with a thin condensing film of condensate.

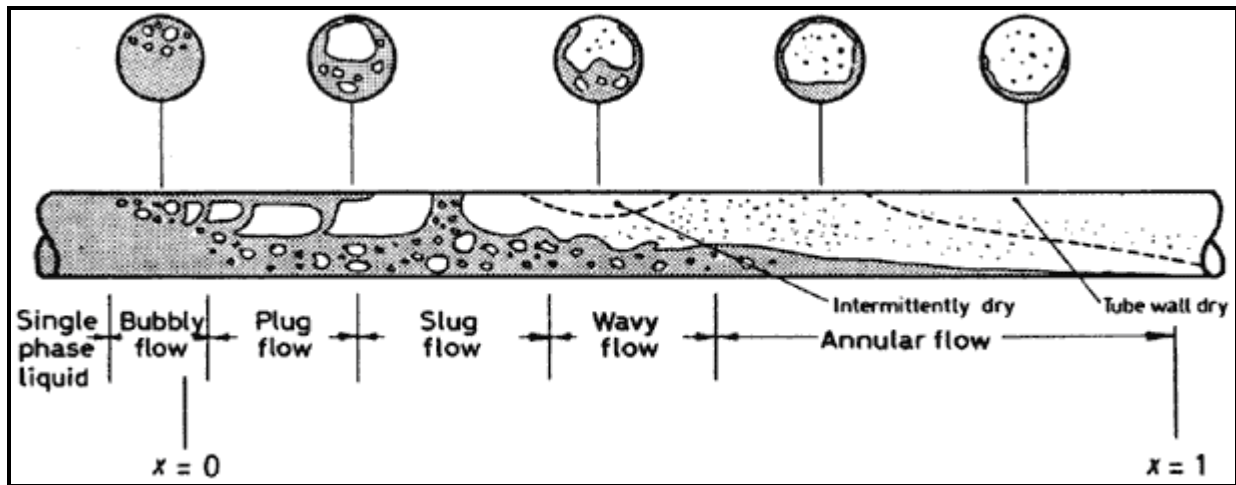


Figure 12.8. Flow patterns during evaporation in a horizontal tube from Collier and Thome (1994).

Kattan-Thome-Favrat map. For small diameter tubes typical of heat exchangers, Kattan, Thome and Favrat (1998a, 1998b, 1998c) proposed a modification of the Steiner (1993) map, which itself is a modified Taitel-Dukler map, and included a method for predicting the onset of dryout at the top of the tube in evaporating annular flows. This flow pattern map will be presented here as it is used in Chapter 10 for predicting local flow boiling coefficients based on the local flow pattern. The flow regime transition boundaries of the Kattan-Thome-Favrat flow pattern map are depicted in Figure 12.9 (bubbly flow is at very high mass velocities and is not shown). This map provides the transition boundaries on a linear-linear graph with mass velocity plotted versus gas or vapor fraction for the particular fluid and flow channel, which is much easier to use than the log-log format of other maps.

The transition boundary curve between *annular and intermittent flows* to *stratified-wavy flow* is:

$$\dot{m}_{\text{wavy}} = \left\{ \frac{16 A_{Gd}^3 g d_i \rho_L \rho_G}{x^2 \pi^2 (1 - (2h_{Ld} - 1)^2)^{0.5}} \left[\frac{\pi^2}{25 h_{Ld}^2} (1-x)^{-F_1(q)} \left(\frac{We}{Fr} \right)_L^{-F_2(q)} + 1 \right] \right\}^{0.5} + 50 \quad [12.4.1]$$

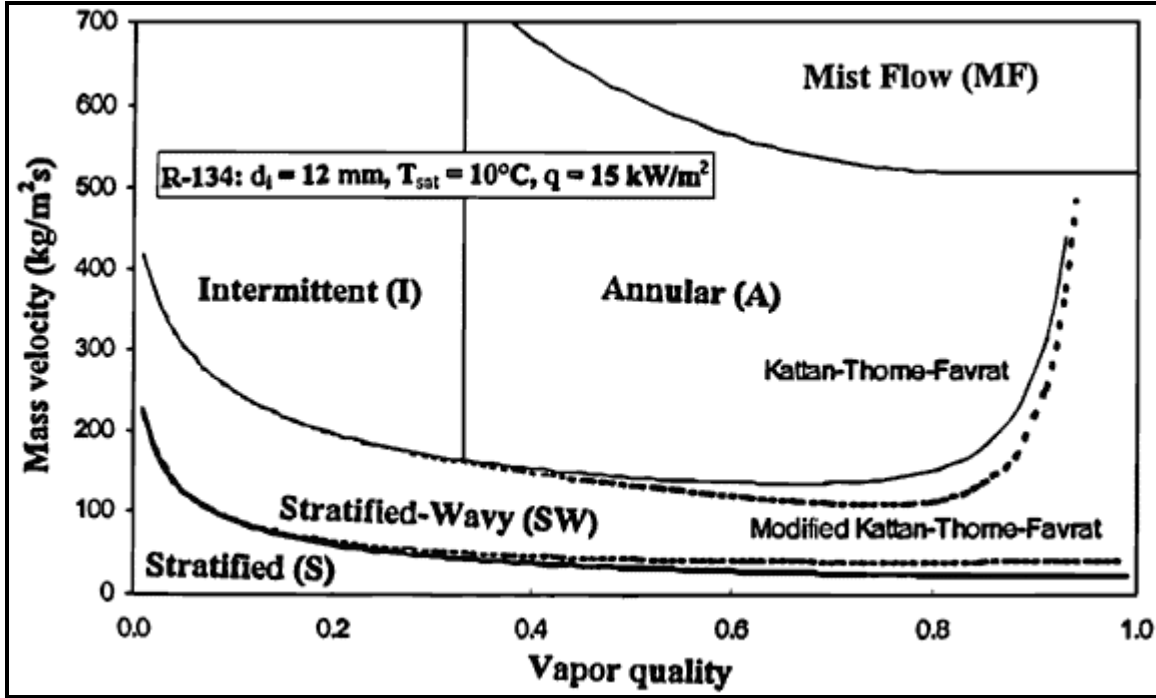


Figure 12.9. Kattan-Thome-Favrat flow pattern map illustrating flow regime transition boundaries.

The high vapor quality portion of this curve depends on the ratio of the Froude number (Fr_L) to the Weber number (We_L), where Fr_L is the ratio of the inertia to the surface tension forces while We_L is the ratio of inertia to gravity forces. The mass velocity threshold for the transition from *annular flow* to *mist flow* is:

$$\dot{m}_{mist} = \left\{ \frac{7680 A_{Gd}^2 g d_i \rho_L \rho_G}{x^2 \pi^2 \xi_{Ph}} \left(\frac{Fr}{We} \right)_L \right\}^{0.5} \quad [12.4.2]$$

Evaluating the above expression for the minimum mass velocity of the mist flow transition gives the value of x_{min} , which for $x > x_{min}$:

$$\dot{m}_{mist} = \dot{m}_{min} \quad [12.4.3]$$

The transition between *stratified-wavy flow* and *fully stratified flow* is given by the expression

$$\dot{m}_{strat} = \left\{ \frac{(226.3)^2 A_{Ld} A_{Gd}^2 \rho_G (\rho_L - \rho_G) \mu_L g}{x^2 (1-x) \pi^3} \right\}^{1/3} \quad [12.4.4]$$

The transition threshold into *bubbly flow* is

$$\dot{m}_{bubbly} = \left\{ \frac{256 A_{Gd} A_{Ld}^2 d_i^{1.25} \rho_L (\rho_L - \rho_G) g}{0.3164 (1-x)^{1.75} \pi^2 P_{id} \mu_L^{0.25}} \right\}^{1/1.75} \quad [12.4.5]$$

In the above equations, the ratio of We to Fr is

$$\left(\frac{We}{Fr}\right)_L = \frac{g d_i^2 \rho_L}{\sigma} \quad [12.4.6]$$

and the friction factor is

$$\xi_{Ph} = \left[1.138 + 2 \log \left(\frac{\pi}{1.5 A_{Ld}} \right) \right]^{-2} \quad [12.4.7]$$

The non-dimensional empirical exponents $F_1(q)$ and $F_2(q)$ in the \dot{m}_{wavy} boundary equation include the effect of heat flux on the onset of dryout of the annular film, i.e. the transition of annular flow into annular flow with partial dryout, the latter which is classified as stratified-wavy flow by the map. They are:

$$F_1(q) = 646.0 \left(\frac{q}{q_{DNB}} \right)^2 + 64.8 \left(\frac{q}{q_{DNB}} \right) \quad [12.4.8a]$$

$$F_2(q) = 18.8 \left(\frac{q}{q_{DNB}} \right) + 1.023 \quad [12.4.8b]$$

The Kutateladze (1948) correlation for the heat flux of departure from nucleate boiling, q_{DNB} is used to normalize the local heat flux:

$$q_{DNB} = 0.13 \rho_G^{1/2} h_{LG} [g(\rho_L - \rho_G) \sigma]^{1/4} \quad [12.4.9]$$

The vertical boundary between *intermittent flow* and *annular flow* is assumed to occur at a fixed value of the Martinelli parameter, X_{tt} , equal to 0.34, where X_{tt} is defined as:

$$X_{tt} = \left(\frac{1-x}{x} \right)^{0.875} \left(\frac{\rho_G}{\rho_L} \right)^{0.5} \left(\frac{\mu_L}{\mu_G} \right)^{0.125} \quad [12.4.10]$$

Solving for x , the threshold line of the intermittent-to-annular flow transition at x_{IA} is:

$$x_{IA} = \left\{ \left[0.2914 \left(\frac{\rho_G}{\rho_L} \right)^{-1/1.75} \left(\frac{\mu_L}{\mu_G} \right)^{-1/7} \right] + 1 \right\}^{-1} \quad [12.4.11]$$

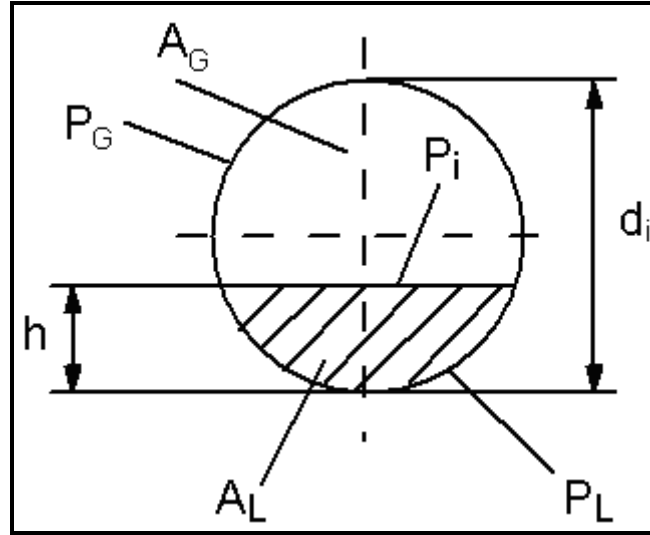


Figure 12.10. Cross-sectional and peripheral fractions in a circular tube.

Figure 12.10 defines the geometrical dimensions of the flow where P_L is the wetted perimeter of the tube, P_G is the dry perimeter in contact with only vapor, h is the height of the completely stratified liquid layer, and P_i is the length of the phase interface. Similarly A_L and A_G are the corresponding cross-sectional areas. Normalizing with the tube internal diameter d_i , six dimensionless variables are obtained:

$$h_{Ld} = \frac{h}{d_i}, \quad P_{Ld} = \frac{P_L}{d_i}, \quad P_{Gd} = \frac{P_G}{d_i}, \quad P_{id} = \frac{P_i}{d_i}, \quad A_{Ld} = \frac{A_L}{d_i^2}, \quad A_{Gd} = \frac{A_G}{d_i^2} \quad [12.4.12]$$

For $h_{Ld} \leq 0.5$:

$$P_{Ld} = \left(8(h_{Ld})^{0.5} - 2(h_{Ld}(1-h_{Ld}))^{0.5} \right) / 3, \quad P_{Gd} = \pi - P_{Ld} \quad [12.4.13]$$

$$A_{Ld} = \left(12(h_{Ld}(1-h_{Ld}))^{0.5} + 8(h_{Ld})^{0.5} \right) h_{Ld} / 15, \quad A_{Gd} = \frac{\pi}{4} - A_{Ld}$$

For $h_{Ld} > 0.5$:

$$P_{Gd} = \left(8(1-h_{Ld})^{0.5} - 2(h_{Ld}(1-h_{Ld}))^{0.5} \right) / 3, \quad P_{Ld} = \pi - P_{Gd} \quad [12.4.14]$$

$$A_{Gd} = \left(12(h_{Ld}(1-h_{Ld}))^{0.5} + 8(1-h_{Ld})^{0.5} \right) (1-h_{Ld}) / 15, \quad A_{Ld} = \frac{\pi}{4} - A_{Gd}$$

For $0 \leq h_{Ld} \leq 1$:

$$P_{id} = 2(h_{Ld}(1-h_{Ld}))^{0.5} \quad [12.4.15]$$

Since h is unknown, an iterative method utilizing the following equation is necessary to calculate the reference liquid level h_{Ld} :

$$X_{tt}^2 = \left[\left(\frac{P_{Gd} + P_{id}}{\pi} \right)^{1/4} \left(\frac{\pi^2}{64 A_{Gd}^2} \right) \left(\frac{P_{Gd} + P_{id}}{A_{Gd}} + \frac{P_{id}}{A_{Ld}} \right) \right] \left(\frac{\pi}{P_{Ld}} \right)^{1/4} \left(\frac{64 A_{Ld}^3}{\pi^2 P_{Ld}} \right) \quad [12.4.16]$$

Once the reference liquid level h_{Ld} is known, the dimensionless variables are calculated from equations [12.4.13] to [12.4.15] and the transition curves for the new flow pattern map are determined with equations [12.4.1] to [12.4.11].

This map was developed from a database for five refrigerants: two single-component fluids (R-134a and R-123), two near-azeotropic mixtures (R-402A and R-404A) and one azeotropic mixture (R-502). The test conditions covered the following range of variables: mass flow rates from 100 to 500 kg/m²s, vapor qualities from 4-100%, heat fluxes from 440 to 36500 W/m², saturation pressures from 0.112 to 0.888 MPa, Weber numbers from 1.1 to 234.5, and liquid Froude numbers from 0.037 to 1.36. The Kattan-Thome-Favrat flow pattern map correctly identified 96.2% of these flow pattern data.

Zürcher, Thome and Favrat (1997c) obtained additional two-phase flow pattern observations for the zeotropic refrigerant mixture R-407C at an inlet saturation pressure of 0.645 MPa and the map accurately identified these new flow pattern data. Zürcher, Thome and Favrat (1999) also obtained two-phase flow pattern data for ammonia with a 14 mm bore sight glass for mass velocities from 20 to 140 kg/m²s, vapor qualities from 1-99% and heat fluxes from 5000 to 58000 W/m², all taken at a saturation temperature of 4°C and saturation pressure of 0.497 MPa. Thus, the mass velocity range in the database was extended from 100 kg/m²s down to 20 kg/m²s. In particular, it was observed that the transition curve \dot{m}_{strat} was too low and Eq. [12.4.4], was empirically corrected by adding +20x as follows:

$$\dot{m}_{strat} = \left\{ \frac{(226.3)^2 A_{Ld} A_{Gd}^2 \rho_G (\rho_L - \rho_G) \mu_L g}{x^2 (1-x) \pi^3} \right\}^{1/3} + 20x \quad [12.4.17]$$

where \dot{m}_{strat} is in kg/m²s. The transition from stratified-wavy flow to annular flow at high vapor qualities was instead observed to be too high and hence an additional empirical term with an exponential factor modifying the boundary at high vapor qualities was added to Equation [12.4.1] to take this into account as:

$$\dot{m}_{wavy(new)} = \dot{m}_{wavy} - 75e^{-\left(\frac{(x^2 - 0.97)^2}{x(1-x)} \right)} \quad [12.4.18]$$

where the mass velocity is in kg/m²s. The movement of these boundaries has an effect on the dry angle calculation θ_{dry} in the Kattan, Thome and Favrat (1998c) flow boiling heat transfer model and shifts the onset of dryout to slightly higher vapor qualities, which is in agreement with the ammonia heat transfer test data.

In addition, Zürcher, Thome and Favrat (1999) found that the onset of dryout effect in the Kattan-Thome-Favrat map was too strong compared to their new, more extensive observations for ammonia. They recommended reducing that the influence by one-half, so the value of q in expressions [12.4.8a] and [12.4.8b] should be replaced with $q/2$.

To utilize this map, the following parameters are required: vapor quality (x), mass velocity (\dot{m}), tube internal diameter (d_i), heat flux (q), liquid density (ρ_L), vapor density (ρ_G), liquid dynamic viscosity (μ_L), vapor dynamic viscosity (μ_G), surface tension (σ), and latent heat of vaporization (h_{LG}), all in SI units. The local flow pattern is identified by the following procedure:

1. Solve Eq. [12.4.16] iteratively with Eqs. [12.4.10], [12.4.13], [12.4.14] and [12.4.15];
2. Evaluate Eq. [12.4.12];
3. Evaluate Eqs. [12.4.6], [12.4.7], [12.4.8a], [12.4.8b] and [12.4.9];
4. Evaluate Eqs. [12.4.1], [12.4.2] or [12.4.3], [12.4.4], [12.4.5] and [12.4.11];
5. Compare these values to the given values of x and \dot{m} to identify the flow pattern.

Note that Eq. [12.4.18] should be used in place of Eq. [12.4.1] and Eq. [12.4.17] should be used in place of Eq. [12.4.11] to utilize the most updated version. The map is thus specific to the fluid properties, flow conditions (heat flux) and tube internal diameter input into the equations. The map can be programmed into any computer language, evaluating the transition curves in incremental steps of 0.01 in vapor quality to obtain a tabular set of threshold boundary points, which can then displayed as a complete map with \dot{m} vs. x as coordinates.

Zürcher-Favrat-Thome map. Following the above work, based on extensive flow pattern observations for ammonia at 5°C in a 14.0 mm horizontal sight glass tube at the exit of the same diameter of evaporator tube, Zürcher, Favrat and Thome (2002) proposed a new version of the transition boundary curve between *annular and intermittent flows* to *stratified-wavy flow*, i.e. for equation [12.4.1], based on an indepth analysis of the dissipation effects in a two-phase flow. The interested reader is referred to their paper for the details.

Thome-El Hajal map. For practicality and for consistency between the flow map and the heat transfer model, an easier to implement version of the Kattan-Thome-Favrat map was proposed by Thome and El Hajal (2003). In the previously presented flow pattern map, dimensionless variables A_{Ld} , A_{Gd} , h_{Ld} and P_{id} were calculated in an iterative way using the stratified flow void fraction model illustrated in Fig.12.10. On the other hand, the flow boiling heat transfer model of Kattan, Thome and Favrat (1998c) uses the Steiner (1993) version of the Rouhani-Axelsson drift flux model for horizontal tubes for the cross-sectional void fraction ε (see Chapter 17):

$$\varepsilon = \frac{x}{\rho_G} \left[(1 + 0.12(1-x)) \left(\frac{x}{\rho_G} + \frac{1-x}{\rho_L} \right) + \frac{1.18(1-x)[g\sigma(\rho_L - \rho_G)]^{0.25}}{\dot{m}\rho_L^{0.5}} \right]^{-1} \quad [12.4.19]$$

This drift flux void fraction model is easy to apply and gives the void fraction as an explicit function of total mass velocity, whereas the iterative method of Taitel and Dukler used previously does not. Hence, it makes sense to use the same void fraction model in both the flow pattern map and the flow boiling heat transfer model. For this, the Rouhani-Axelsson model is a good choice as the general method, at least for refrigerants, which has been proven experimentally by 238 void fraction measurements for R-22 and R-410A made by Ursenbacher, Wojtan and Thome (2004) for stratified-wavy and intermittent types of flow. Using this void fraction model, the values A_{Ld} and A_{Gd} are now directly determinable by first calculating the void fraction using the above expression:

$$A_{Ld} = \frac{A(1-\varepsilon)}{d_i^2} \quad [12.4.20]$$

$$A_{Gd} = \frac{A\varepsilon}{d_i^2} \quad [12.4.21]$$

The dimensionless liquid height h_{Ld} and the dimensionless length of the liquid interface P_{id} can be expressed as a function of the stratified angle θ_{strat} (stratified angle around upper perimeter of the tube to stratified liquid level):

$$h_{Ld} = 0.5 \left[1 - \cos \left(\frac{2\pi - \theta_{strat}}{2} \right) \right] \quad [12.4.22]$$

$$P_{id} = \sin \left(\frac{2\pi - \theta_{strat}}{2} \right) \quad [12.4.23]$$

To avoid completely any iteration, the geometrical expression for the stratified angle θ_{strat} is calculated from an approximate expression by Biberg (1999), evaluated in terms of void fraction, as follows:

$$\theta_{strat} = 2\pi - 2 \left\{ \begin{array}{l} \pi(1 - \varepsilon) + \left(\frac{3\pi}{2} \right)^{1/3} \left[1 - 2(1 - \varepsilon) + (1 - \varepsilon)^{1/3} - \varepsilon^{1/3} \right] \\ - \frac{1}{200} (1 - \varepsilon) \varepsilon [1 - 2(1 - \varepsilon)] [1 + 4((1 - \varepsilon)^2 + \varepsilon^2)] \end{array} \right\} \quad [12.4.24]$$

As the void fraction is a function of mass velocity, it influences the position of the transition curves that involve ε in the Thome-El Hajal map. The effect of mass velocity on flow regime transitions is shown in Figure 12.11, where the influence is only significant at low mass velocities. The strongest effect of mass velocity is observed on the SW-I/A transition curve for vapor qualities below 0.1 and at very low mass velocities, where the transition curve goes up with increasing mass velocity. This divergence becomes less significant as the vapor quality increases and at higher mass velocities. The boundary curve A-M also moves up marginally with increasing mass velocity. In implementing the method for design purposes, the actual mass velocity is used to calculate the transition curves while for expediency in calculating the flow pattern maps below, a fixed value of mass velocity was used for evaluating the entire map.

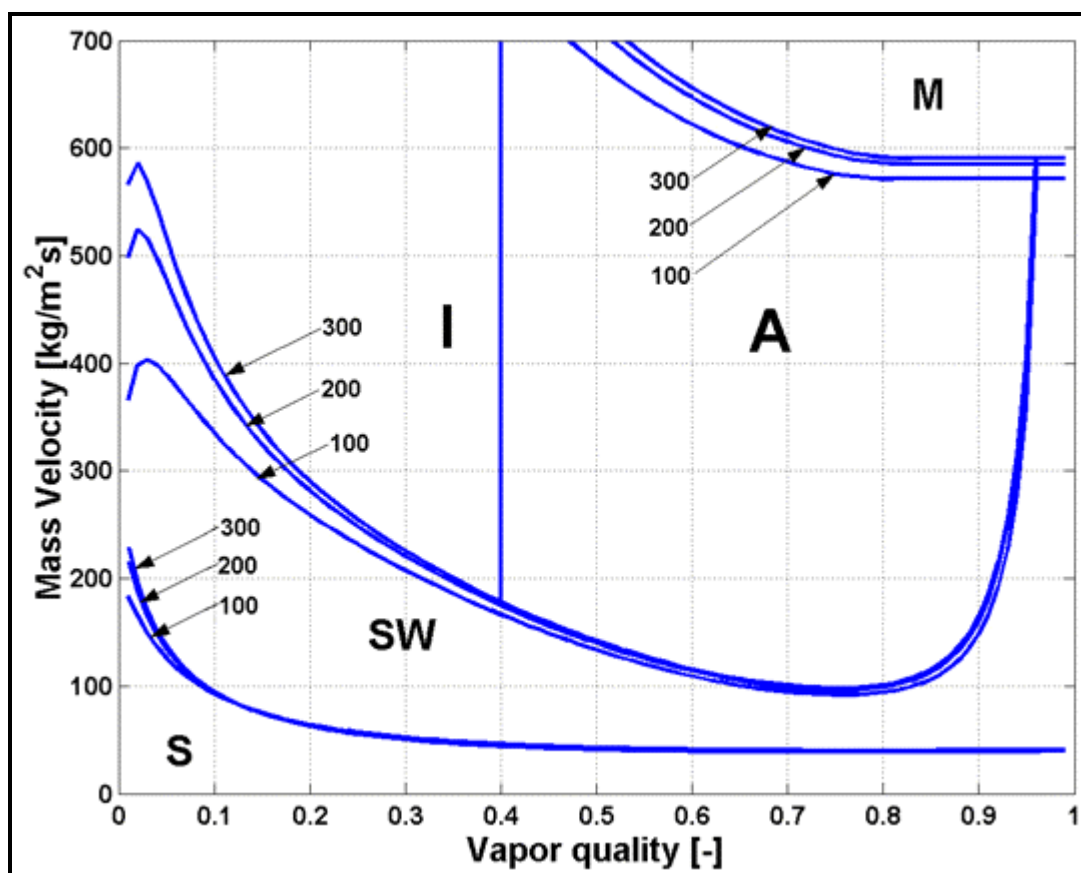


Figure 12.11. Flow pattern map of Thome-El Hajal for R-410A at 5°C in a 13.84 mm internal diameter tube with its equations evaluated at mass velocities of 100, 200 and 300 kg/m²s at a heat flux of 17.5 kW/m².

Some high quality photographs of two-phase flow patterns in horizontal tubes are available from Barbieri, Sáiz-Jabardo and Bandarra Filho (2005) taken in the test facility described in Barbieri and Sáiz-Jabardo (2006). They are for 500 kg/m²s for R-134a in a sight glass tube at the exit of an evaporator tube (note some external condensation on the outside of the tube in some of the photographs). Figure 12.12 shows some high quality photographs of stratified types of flow. Figure 12.13 shows the sequence of events in the intermittent flow regime, characterized by a cyclic variation between low amplitude waves (top photograph) and large amplitude waves (bottom photograph). Figure 12.14 presents some images of annular flow.

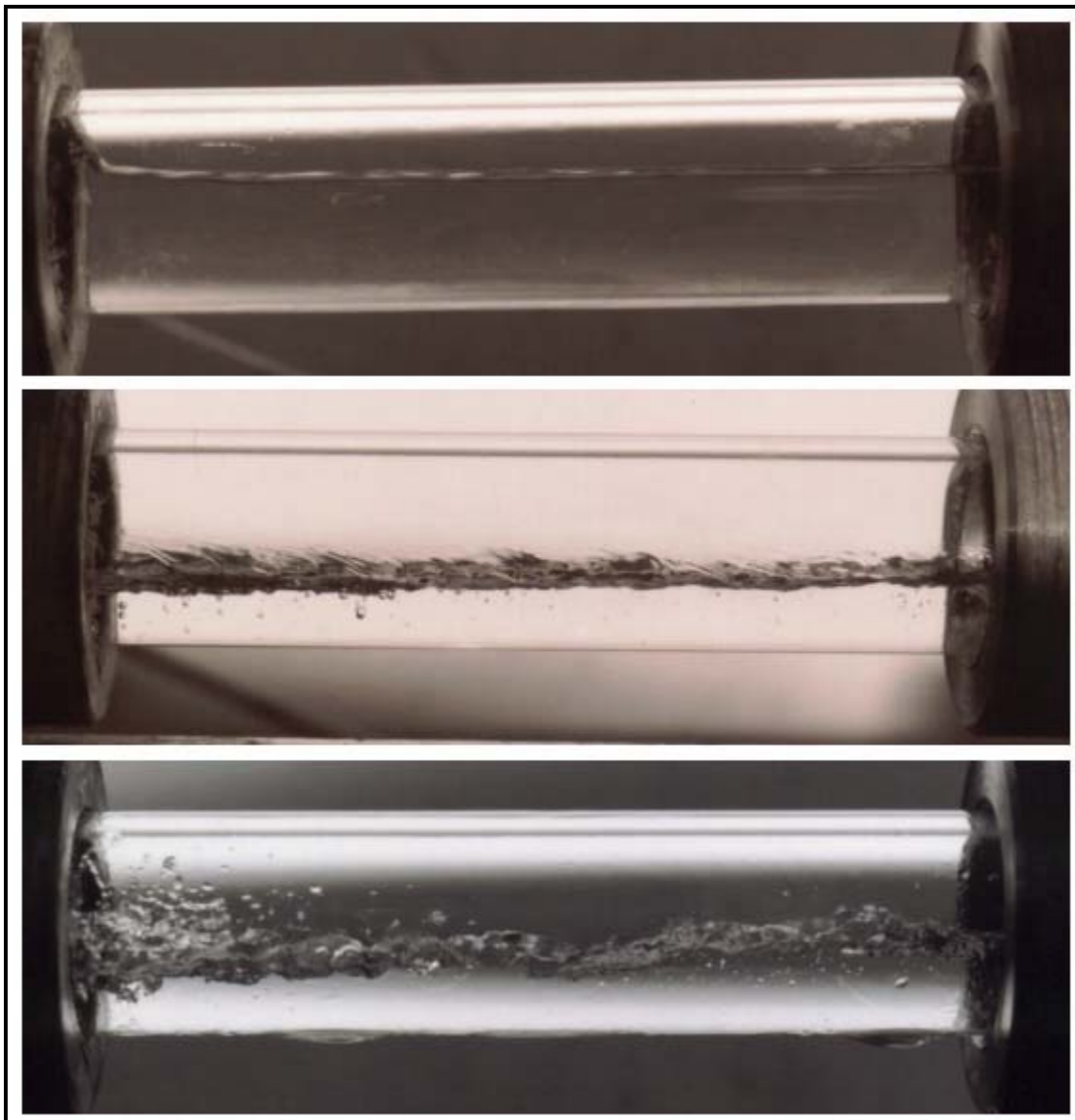


Figure 12.12. Stratified flow regime photographs of Barbieri, Sáiz-Jabardo and Bandarra Filho (2005). Top: stratified flow; middle and bottom: stratified-wavy flow. Tube diameter: 15.8 mm.

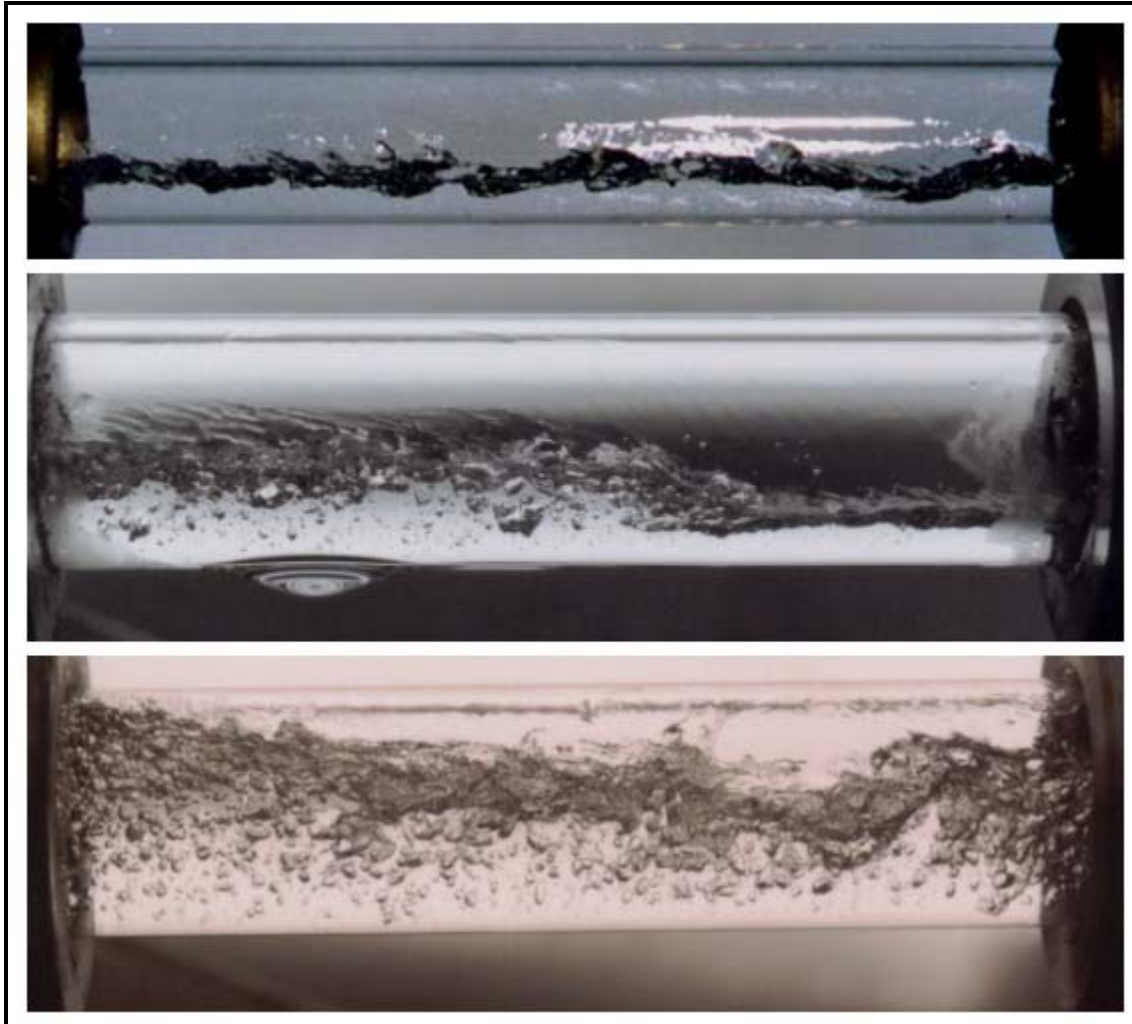


Figure 12.13. Intermittent flow regime photographs of Barbieri, Sáiz-Jabardo and Bandarra Filho (2005) with a sequence of interfacial waves in a 9.52 mm tube (top) followed by climbing waves in a 15.8 mm tube (middle) and then a large amplitude wave reaching the top of the channel in a 15.8 mm tube (bottom).

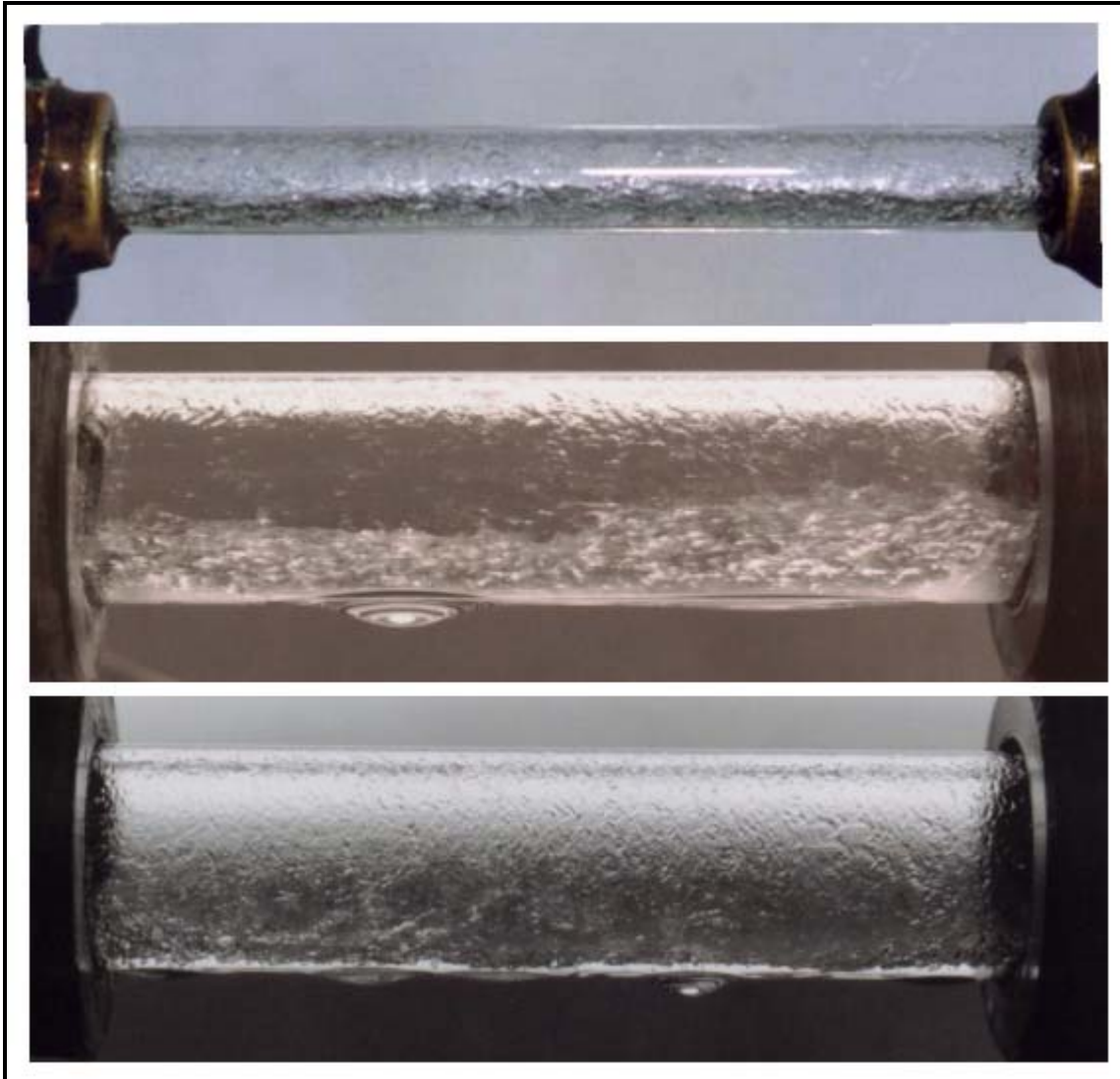


Figure 12.14. Annular flow regime photographs of Barbieri, Sáiz-Jabardo and Bandarra Filho (2005) showing three images of the interfacial waves on an annular liquid film. Top: 9.52 mm tube; middle: 15.8 mm tube; bottom: 15.8 mm tube.

Wojtan-Ursenbacher-Thome map. The flow pattern map of Kattan, Thome and Favrat (1998a) was developed primarily for vapor qualities higher than 0.15 and also without benefit of a dedicated experimental campaign on the effect of heat flux on the initiation and completion of dryout at high vapor qualities. In light of the dynamic void fraction measurements made by Wojtan, Ursenbacher and Thome (2004) and their video observations for mass velocities between 70-200 kg/m²s in a 13.84 mm horizontal sight glass tube, the following conclusions were reached:

1. Fully stratified flow was not detected at any of the mass velocities tested;
2. In the vapor quality range $0 < x < x_{IA}$, an alternating flow structure of liquid slugs and stratified-wavy interfaces was observed (where x_{IA} is the vertical line separating intermittent and annular flows);
3. The transition from slug/stratified-wavy flows to fully stratified-wavy flows without any slugs appeared approximately to occur at x_{IA} ;

- Only slug flow was observed for the zone identified by the Thome-El Hajal map to be in the stratified-wavy region for $\dot{m} > \dot{m}_{wavy}(x_{IA})$.

Based on these observations, the stratified-wavy flow region of the Thome-El Hajal version of the flow map was modified by Wojtan, Ursenbacher and Thome (2005a) as follows:

- A new transition line was added at $\dot{m}_{strat} = \dot{m}_{strat}(x_{IA})$ at $x < x_{IA}$ (this creates a new horizontal transition line to the left of x_{IA} and modifies the boundary of the stratified (S) regime);
- The stratified-wavy region has been divided into three subzones:
 - For $\dot{m} > \dot{m}_{wavy}(x_{IA})$, this becomes the Slug zone.
 - For $\dot{m}_{strat} < \dot{m} < \dot{m}_{wavy}(x_{IA})$ and $0 < x < x_{IA}$, this becomes the Slug/Stratified-Wavy zone.
 - For $1 > x \geq x_{IA}$, this remains as the Stratified-Wavy zone.

Figure 12.15 depicts the new flow pattern map calculated for R-22 with the above modifications applied to the Thome-El Hajal version of Kattan-Thome-Favrat flow pattern map to better describe the actual character of the flow. The dash lines correspond to the new dryout and mist flow transition curves described below.

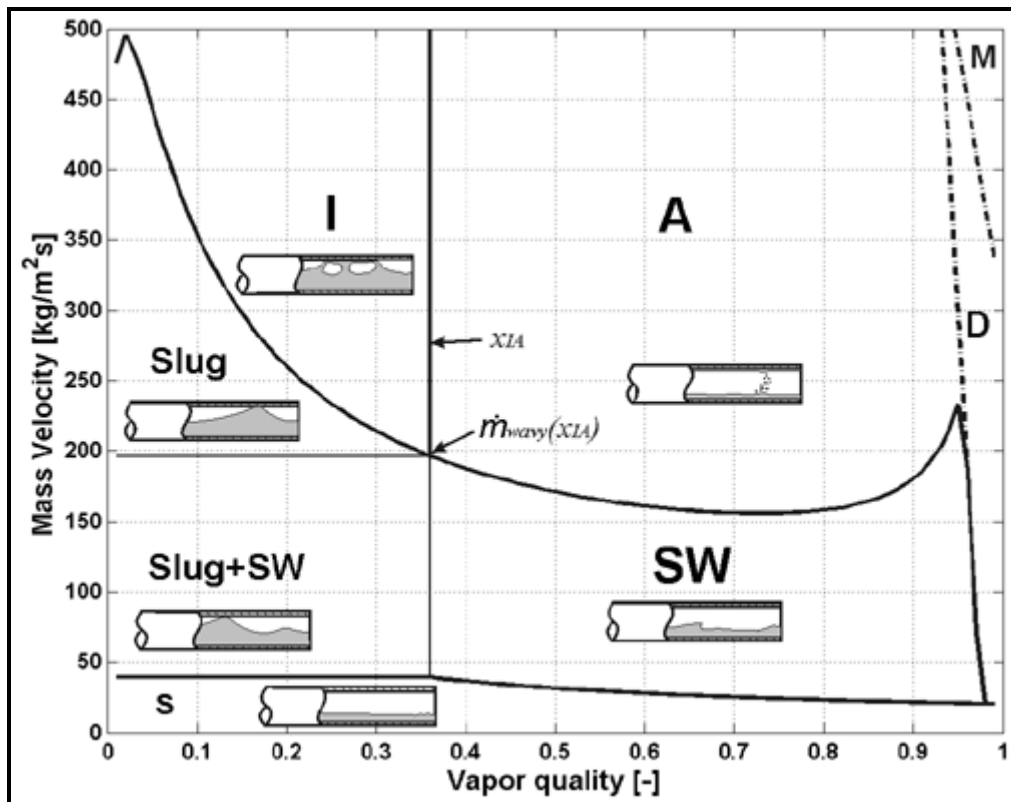


Figure 12.15. New flow pattern map simulated for R-22 at 50C in a 13.84 mm channel using 100 kg/m²s and 2.1 kW/m² to calculate the transition curves.

As depicted in Figure 12.16, dryout occurs at the top of a horizontal tube first at x_{di} (cross section A-A), where the annular liquid film is thinner, and then dryout proceeds around the perimeter of the tube along its length (cross section B-B) until reaching the bottom (cross section C-C) where the liquid film disappears at x_{de} . Thus, dryout in a horizontal tube takes place over a range of vapor qualities, beginning

as an annular flow and ending when the fully developed mist flow regime is reached. This flow regime between x_{di} and x_{de} is called dryout.

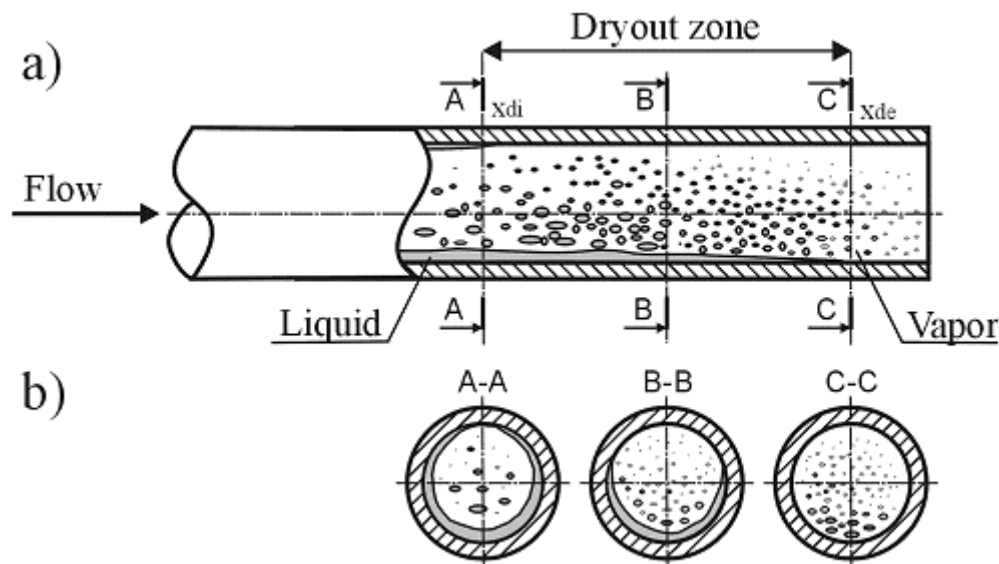


Figure 12.16. Dryout in a horizontal tube. (a) Dryout zone during evaporation in a horizontal tube beginning at x_{di} at top of tube and ending at x_{de} at bottom of tube; (b) Cross sections: A-A onset of dryout in annular flow; B-B dryout; C-C end of dryout and beginning of mist flow.

Since it is difficult to determine the onset and completion of dryout only from visual observations in a sight glass tube, a large number of experimental flow boiling heat transfer points were measured by Wojtan, Ursenbacher and Thome (2005a) for R-22 and R-410A at mass velocities from 70 to 700 kg/m²s and heat fluxes from 2.0 to 57.5 kW/m². The tube internal diameters tested were 13.84 mm for R-22 and R-410A as well as 8.00 mm for R-410A. These flow boiling heat transfer data were used to identify the locations of x_{di} and x_{de} . As illustrated in Figure 12.17, the sharp change in the heat transfer coefficient with increasing vapor quality indicates the inception of dryout whereas the end of this decrease of heat transfer coefficient marks the end of dryout and the beginning of mist flow. The observations in the sight glass confirmed that the onsets of dryout and mist flow appeared at the same vapor quality as detected by the heat transfer measurements.

Analyzing experimental results and observations in the sight glass, it is obvious that usually there is no step-wise transition from annular flow to mist flow. The first attempt to model the annular-dryout transition during evaporation in horizontal tubes was made by Lavin and Young (1965). They proposed a new transition between the annular and dryout zones based on the Weber number for R-22 and R-12. Lavin and Young observed the dryout process, but with the apparatus used, they could not obtain the heat transfer coefficient within the dryout regime nor study the conditions under which the dryout regime ends and a stable mist flow was established.

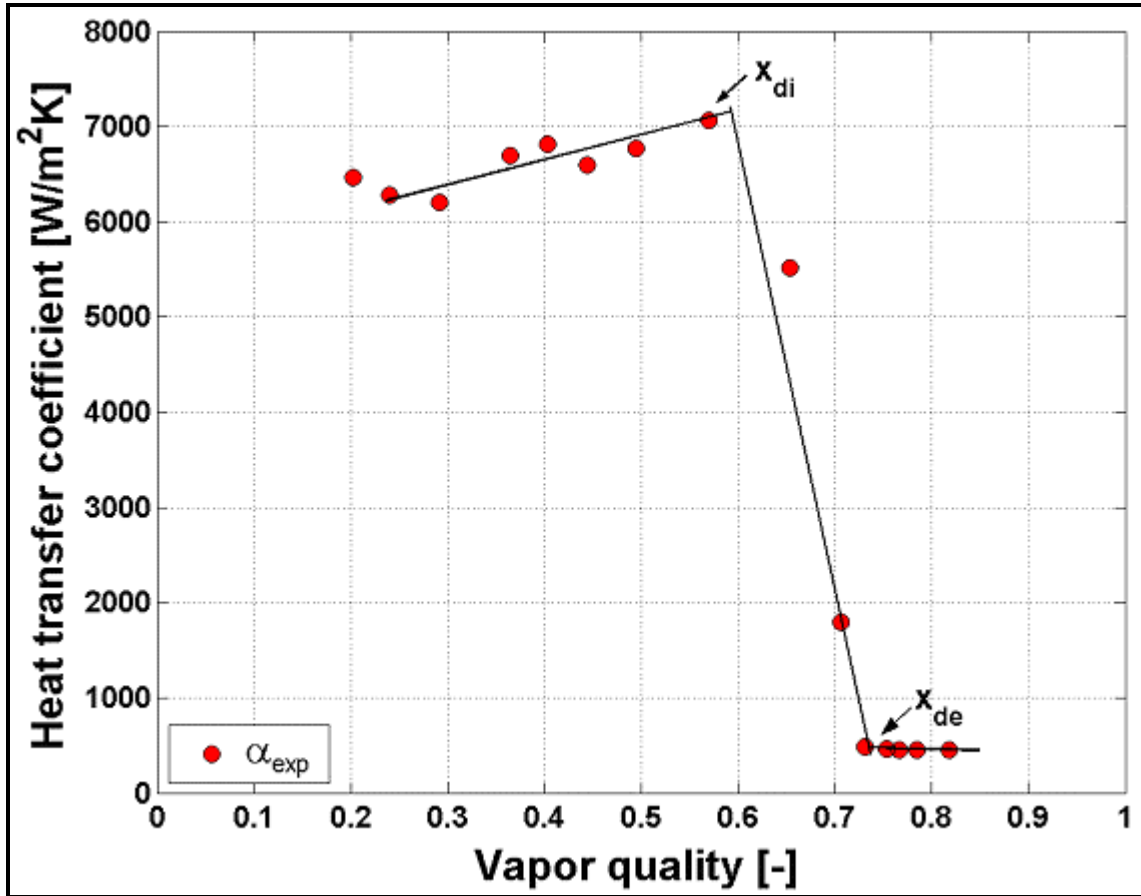


Figure 12.17. Experimental heat transfer coefficients in the 13.84 mm test section for R-22 at 5°C with an initial heat flux of 57.5 kW/m² at 600 kg/m²s.

Since dryout occurs over an interval of vapor quality, Mori et al. (2000) defined the inception of dryout to be x_{di} and the completion of dryout to be x_{de} and then used three characteristic regimes that they named $S1$, $S2$ and $S3$ to predict their values. The best agreement of the Wojtan, Ursenbacher and Thome (2005a) values of x_{di} and x_{de} identified from their heat transfer data were given by their regime $S2$, whose corresponding transition expressions by Mori et al. (2000) are:

$$x_{di} = 0.58 e^{[0.52 - 0.000021 We_G^{0.96} Fr_G^{-0.02} (\rho_G/\rho_L)^{-0.08}]}$$
 [12.4.25]

$$x_{de} = 0.61 e^{[0.57 - 0.0000265 We_G^{0.94} Fr_G^{-0.02} (\rho_G/\rho_L)^{-0.08}]}$$
 [12.4.26]

The approach of Mori et al. was modified by Wojtan, Ursenbacher and Thome (2005a) to include the heat flux effect observed from their results for R-22 and R-410A evaporating at 5°C in 8.00 and 13.84 mm diameter test sections for heat fluxes up to 57.5 kW/m², using the dimensionless heat flux ratio (q/q_{DNB}) and new empirical factors. Thus, the new limits for the beginning and end of the dryout regime are calculated with their following transition equations:

$$x_{di} = 0.58 e^{[0.52 - 0.235 We_G^{0.17} Fr_G^{0.37} (\rho_G/\rho_L)^{0.25} (q/q_{DNB})^{0.7}]}$$
 [12.4.27]

$$x_{de} = 0.61 e^{[0.57 - 0.0058 We_G^{0.38} Fr_G^{0.15} (\rho_G/\rho_L)^{-0.09} (q/q_{DNB})^{0.27}]} \quad [12.4.28]$$

where q_{DNB} is calculated with the expression [12.4.9] of Kutateladze (1948). After inversion of these two equations to solve for the mass velocity in terms of vapor quality, the annular-to-dryout boundary (A-D) and the dryout-to-mist flow boundary (D-M) transition equations for x_{di} and x_{de} become respectively:

$$\dot{m}_{dryout} = \left[\frac{1}{0.235} \left(\ln \left(\frac{0.58}{x} \right) + 0.52 \right) \left(\frac{d_i}{\rho_G \sigma} \right)^{-0.17} \left(\frac{1}{gd_i \rho_G (\rho_L - \rho_V)} \right)^{-0.37} \left(\frac{\rho_G}{\rho_L} \right)^{-0.25} \left(\frac{q}{q_{DNB}} \right)^{-0.7} \right]^{0.926} \quad [12.4.29]$$

$$\dot{m}_{mist} = \left[\frac{1}{0.0058} \left(\ln \left(\frac{0.61}{x} \right) + 0.57 \right) \left(\frac{d_i}{\rho_G \sigma} \right)^{-0.38} \left(\frac{1}{gd_i \rho_G (\rho_L - \rho_V)} \right)^{-0.15} \left(\frac{\rho_G}{\rho_L} \right)^{0.09} \left(\frac{q}{q_{DNB}} \right)^{-0.27} \right]^{0.943} \quad [12.4.30]$$

Including the above modifications also to the stratified-wavy region and integrating the new A-D and D-M transition curves into their map, the implementation procedure for the Wojtan-Ursenbacher-Thome map is as follows:

1. The geometric parameters ε , A_{Ld} , A_{Gd} , h_{Ld} , P_{id} and θ_{strat} are calculated using the expressions [12.4.19] to [12.4.24], respectively.
2. As the effect of heat flux at high vapor quality is captured by the A-D and D-M transition curves, the SW-I/A transition is first calculated from the following adiabatic version of expression [12.4.1]:

$$\dot{m}_{wavy} = \left\{ \frac{16 A_{Gd}^3 gd_i \rho_L \rho_G}{x^2 \pi^2 [1 - (2h_{Ld} - 1)^2]^{0.5}} \left[\frac{\pi^2}{25 h_{Ld}^2} \left(\frac{We_L}{Fr_L} \right)^{-1} + 1 \right] \right\}^{0.5} + 50 \quad [12.4.31]$$

3. The stratified-wavy region is then subdivided into three zones as follows:
 - i. $\dot{m} > \dot{m}_{wavy}(x_{IA})$ gives the slug flow zone;
 - ii. $\dot{m}_{strat} < \dot{m} < \dot{m}_{wavy}(x_{IA})$ and $0 < x < x_{IA}$ give the Slug/Stratified-Wavy zone;
 - iii. $1 > x \geq x_{IA}$ gives the Stratified-Wavy zone.
4. The S-SW transition is calculated from the original boundary expression [12.4.4] but now $\dot{m}_{strat} = \dot{m}_{strat}(x_{IA})$ when $x < x_{IA}$, the latter which gives the flat horizontal part of the boundary for $0 \leq x \leq x_{IA}$.
5. The I-A transition is calculated from the original boundary given by [12.4.11] and extended down to its intersection with \dot{m}_{strat} .
6. The A-D boundary is calculated from [12.4.29] where its value takes precedent over the value from step 2 above when its value is smaller than \dot{m}_{wavy} .

7. The D-M boundary is calculated from [12.4.30] but since the A-D and D-M lines are not parallel these boundaries can intersect, so that when $x_{de} < x_{di}$ then x_{de} is set equal to the value of x_{di} and no D region exists (at high mass velocities and low heat fluxes where this occurs, the high vapor shear will tend to make the annular film to be of uniform thickness and hence it seems reasonable that the entire perimeter becomes dry simultaneously at x_{di}).
8. The following logic is applied to define the transitions in the high vapor quality range for the onset of dryout in the map, referred to as \dot{m}_{dryout} , implemented in the following order:
 - If $\dot{m}_{strat}(x) \geq \dot{m}_{dryout}(x)$, then $\dot{m}_{dryout} = \dot{m}_{strat}(x)$;
 - If $\dot{m}_{wavy}(x) \geq \dot{m}_{dryout}(x)$, then $\dot{m}_{dryout} = \dot{m}_{dryout}(x)$ and the \dot{m}_{wavy} curve ceases to exist, which means that the rightmost boundary of the \dot{m}_{wavy} curve is its intersection with the \dot{m}_{dryout} curve;
 - If $\dot{m}_{dryout}(x) \geq \dot{m}_{mist}(x)$, which is possible at low heat fluxes and high mass velocities, then $\dot{m}_{dryout} = \dot{m}_{dryout}(x)$ and the dryout regime disappears at this mass velocity.

Figure 12.18 shows the flow pattern maps calculated for R-22 for four heat fluxes, where the movements of the A-D and D-M boundaries are quite evident. Compared to the Kattan-Thome-Favrat map, the new regimes slug (Slug), slug/stratified-wavy (Slug+SW) and dryout (D) are now encountered. Notably, it is observed that the dryout and mist flow regions become smaller as the heat flux decreases.

This map was developed from a database for R-22 and R-410A at 5°C but its prior versions covered eight other refrigerants (R-134a, R-123, R-402A, R-404A, R-502, R-407C, R-507A and ammonia) for tube diameters from 8 to 14 mm. The test conditions in all these experiments covered the following range of variables: mass flow rates from 16 to 700 kg/m²s, vapor qualities from 1-99% and heat fluxes from 440 to 57500 W/m². It is believed that the map is appropriate for refrigerants (and fluids with similar physical properties such as light hydrocarbons) at low to medium pressures but not for CO₂ (too high of operating pressures for the map) nor for air-water or steam-water systems (their surface tension and density ratio are too high with respect to the refrigerant database).

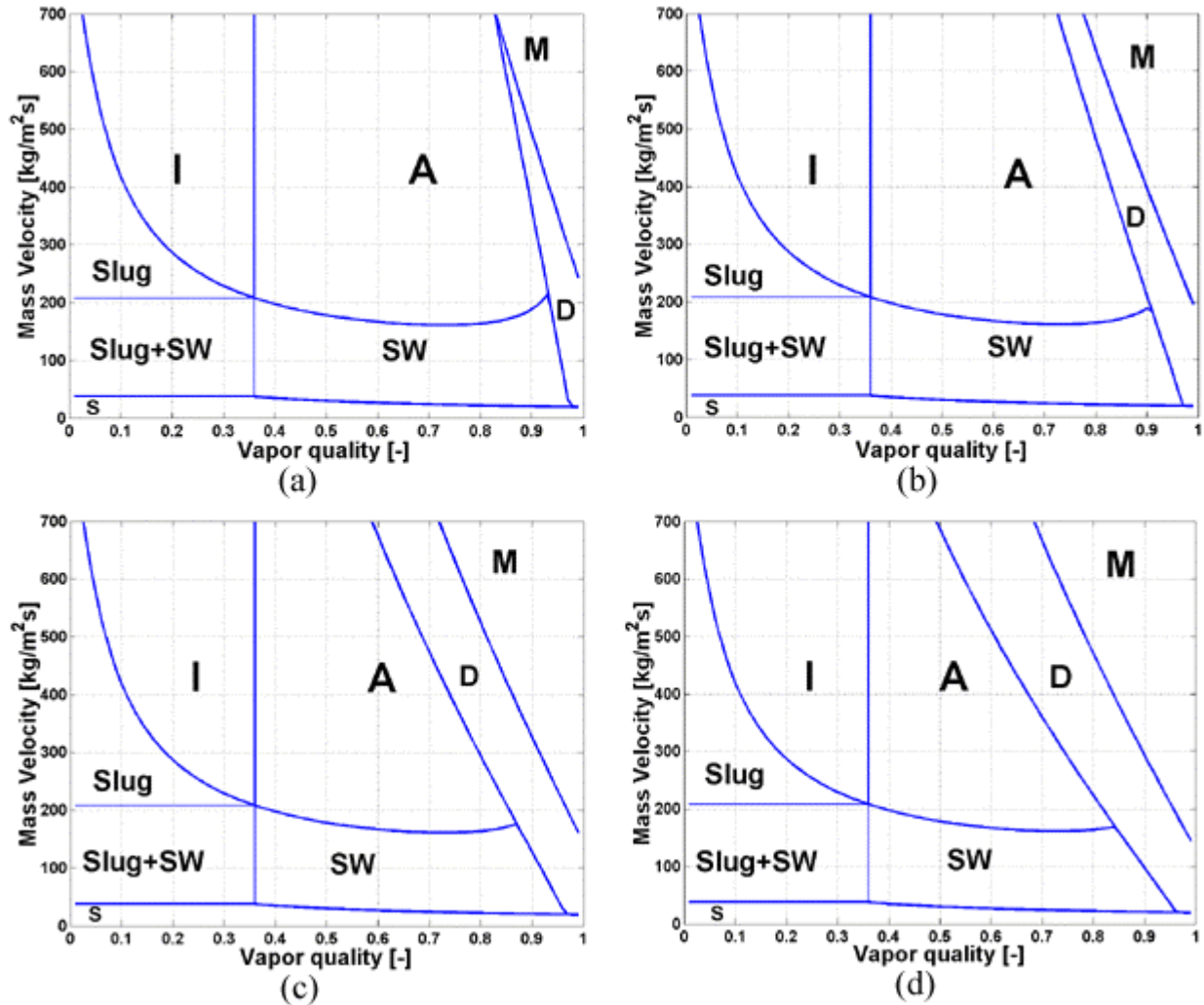


Figure 12.18. Flow pattern maps for R-22 at 5°C in a 13.84 mm tube evaluated at 300 kg/m²s for four heat fluxes: a) 7.5 kW/m², b) 17.5 kW/m², c) 37.5 kW/m², d) 57.5 kW/m².

12.4.1 Example flow pattern maps for selected fluids for evaporation in horizontal tubes

Figure 12.19 displays various flow pattern maps calculated with the most recent version of the Thome and coworkers flow pattern maps described above for the hydrocarbon fluids n-butane and propane. The conditions of the calculations are listed in the maps where the flow regimes shown are: Mist Flow (MF), Intermittent (I), Annular (A), Stratified-Wavy (SW) and Stratified (S). The bubbly flow regime is not depicted as it occurs at much larger mass velocities than those shown.

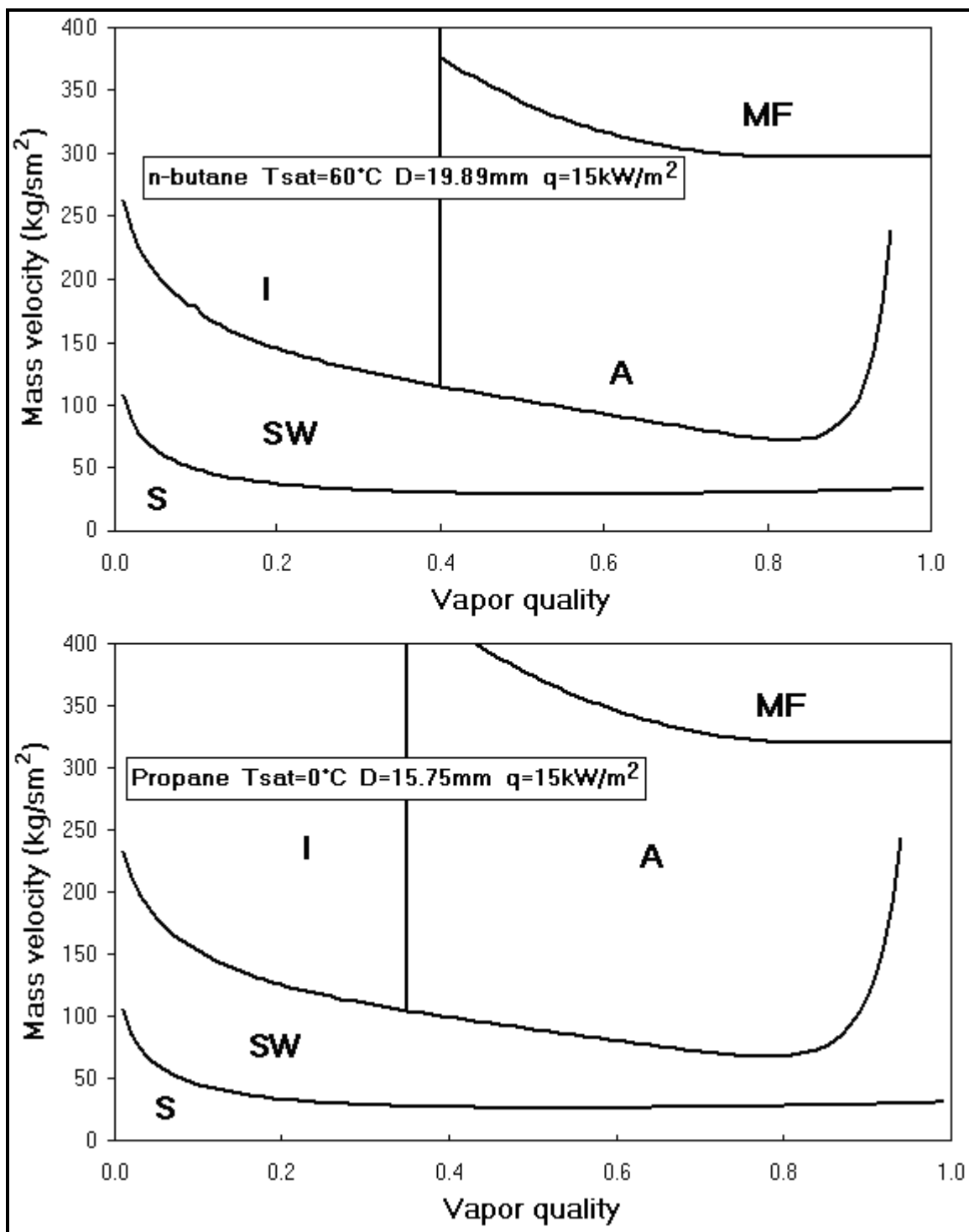


Figure 12.19. Flow pattern map for n-butane and propane evaporating in a horizontal tube.

12.5 Flow Pattern Map for Condensation in Horizontal Tubes

Flow patterns that occur during condensation inside horizontal tubes are similar to those for evaporation described in the previous section with the following exceptions:

1. Dry saturated vapor is entering the tube and hence the process begins without any entrainment of liquid while for evaporating flows the liquid bridging across the flow channel in churn and intermittent flow can result in significant entrainment when these flow structures break up.
2. During evaporation, the annular film eventually dries out while for condensation no dryout occurs. In fact, for condensation at high vapor qualities the flow is annular and there is no passage from stratified-wavy flow into annular flow while for evaporation the flow reverts to stratified-wavy flow at the onset of dryout at the top of the tube.
3. During condensation, the condensate formed coats the tube perimeter with a liquid film. In what would otherwise be a mist flow for adiabatic or evaporating flows, in condensation the flow regime will look like annular flow since the entrainment of liquid into the vapor core will leave bare surface available for rapid formation of a new liquid layer via condensation.
4. During condensation in stratified flow regimes, the top of the tube is wetted by the condensate film while in adiabatic and evaporating flows the top perimeter is dry.

Hence, the three principal flow patterns encountered during condensation inside horizontal tubes are:

- Annular flow (often referred to as the shear-controlled regime in condensation heat transfer literature);
- Stratified-wavy flow (characterized by waves on the interface of the stratified liquid flowing along the bottom of the tube with film condensation on the top perimeter);
- Stratified flow (no interfacial waves on the stratified liquid flowing along the bottom of the tube with film condensation on the top perimeter that drains into the stratified liquid).

The latter are sometimes referred to as the gravity-controlled regime in condensation heat transfer literature. These flow regimes can tentatively be predicted using the Kattan-Thome-Favrat flow pattern maps for intube evaporation as proposed by El Hajal, Thome and Cavallini (2003). First, the mist flow transition is eliminated because flow in this zone may be considered to be annular flow since a condensate film is always formed, even if the liquid is then entrained. Secondly, the stratified-wavy transition curve is modified by first eliminating the transition from annular flow to stratified-wavy flow at high vapor qualities by solving for the minimum in the stratified-wavy flow transition curve and then extending this curve as a straight line from that point to the end of the stratified transition curve for \dot{m}_{strat} at a vapor quality of $x = 1.0$. Figure 12.20 illustrates this flow pattern map for condensation of R-134a at 40°C in a horizontal tube of 8.0 mm internal diameter.

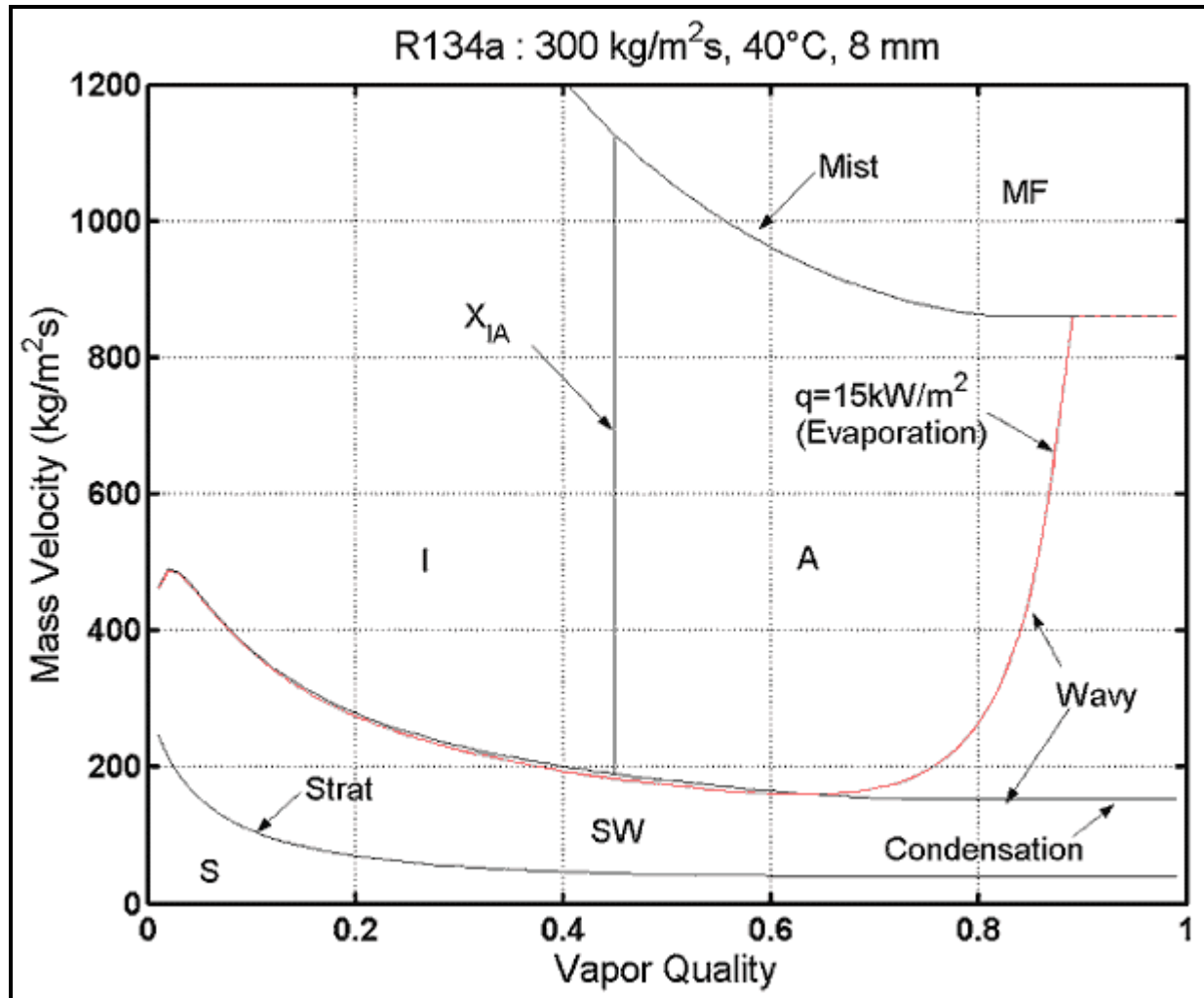


Figure 12.20. Flow pattern map for intube condensation of R-134a at 40°C in a horizontal tube of 8.0 mm internal diameter by El Hajal, Thome and Cavallini (2003).

Soliman (1982) also proposed a method for prediction of the transition from annular flow to stratified-wavy flow during condensation inside horizontal tubes. Refer to Chapter 8 for a description of his method that was used by Dobson and Chato (1998) in their intube condensation heat transfer model.

12.6 Flow Patterns in Horizontal Enhanced Tubes

Not many systematic flow pattern studies on two-phase flows in internally enhanced tubes have been undertaken, although it is thought that an enhancement can have a significant effect of the location of flow pattern transitions and can also change what a flow pattern looks like. For instance, it is thought that an internally microfinned tube will decrease the annular to stratified-wavy flow threshold to lower mass velocities, hence increasing heat transfer at lower mass velocities by achieving complete wetting of the tube perimeter. For instance, visual observations of Cavallini et al. (2002) have confirmed this hypothesis, whose comparative videos can be seen in Chapter 1.

Some videos illustrating two-phase flows inside a plain glass tube with a twisted tape insert by Moreno Quiben and Thome can also be seen in Chapter 1, where a swirl effect is seen to be imparted on the flow.

Again, it is believed that the annular-stratified wavy transition threshold \dot{m}_{wavy} is displaced to lower mass velocities, but this was not systematically documented, however.

Within annular flow itself, microfins create more turbulence in the liquid film as shown in Figure 12.21 with photographs provided by Sáiz-Jabardo (2005) using the test facility described in Bandarra Filho and Sáiz-Jabardo (2006). It appears from the photographs that the microfin tube also increases liquid entrainment in the central vapor core (the photographs are for a smooth sight glass tube at the exit of the evaporator tubes so the direct effect of the microfins cannot be seen).

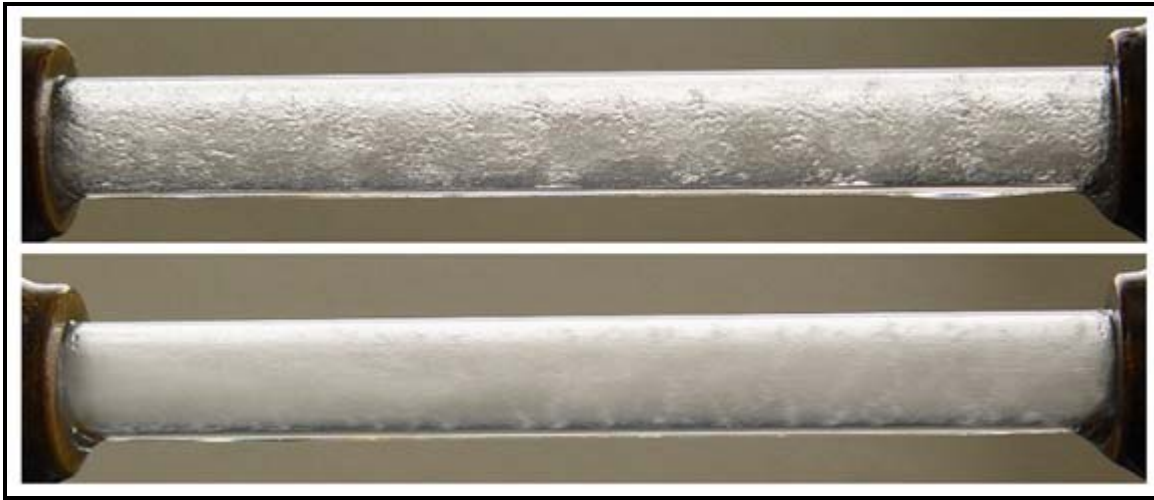


Figure 12.21. Annular flow patterns for R-134a at 5°C and 500 kg/m²s from Bandarra Filho and Sáiz-Jabardo (2006) at the exit of an evaporator tube. Top photo: smooth tube; bottom photo: microfin tube. Tube diameter: 9.52 mm.

Bukasa, Liebenberg and Meyer (2004), Olivier et al. (2004), Liebenberg, Thome and Meyer (2005) and Olivier et al. (2007) have investigated flow patterns in a plain tube, a helical microfin tube (Wolverine Tube), a herringbone microfin tube (Wolverine Tube) and a tube with helical wire inserts. Meyer and Liebenberg (2006) have also summarized this work in a state-of-the-art review paper. While finding that the intermittent-to-annular flow transition equation [12.4.11] for x_{IA} worked well for their smooth bore tube, they found that an internal enhancement delayed the transition to lower vapor qualities for the microfin tubes during the condensation of R-22, R-134a and R-407C, as depicted in Figure 12.22. They observed the flow patterns directly at the exit of their condensation test sections in that study while also using a power-spectral analysis of the absolute pressure signal to identify the transitions in previous studies. In their most recent tests, helical wires with axial pitches of 5.0, 7.7 and 11.0 mm were tested. While the wire insert displaced the x_{IA} transition to lower vapor qualities, they on the other hand found little effect of the wire pitch itself on the location of the x_{IA} transition boundary. In these tests with wires, the internal tube diameter was 8.1 mm and the wire diameter was 0.5 mm.

Based on their results, Meyer, Liebenberg and coworkers proposed the following expression for the transition x_{IA} for the intermittent-to-annular flow transition line for tubes with such helical wire inserts:

$$x_{IA} = \left\{ \left[0.484 \left(\frac{\rho_G}{\rho_L} \right)^{-5/9} \left(\frac{\mu_L}{\mu_G} \right)^{-1/9} \right] + 1 \right\}^{-1} \quad [12.6.1]$$

Similar transition lines for the helical microfin and herringbone microfin tubes were also proposed, with values of 0.678 and 0.790 in place of 0.484, respectively, in their earlier studies mentioned above.

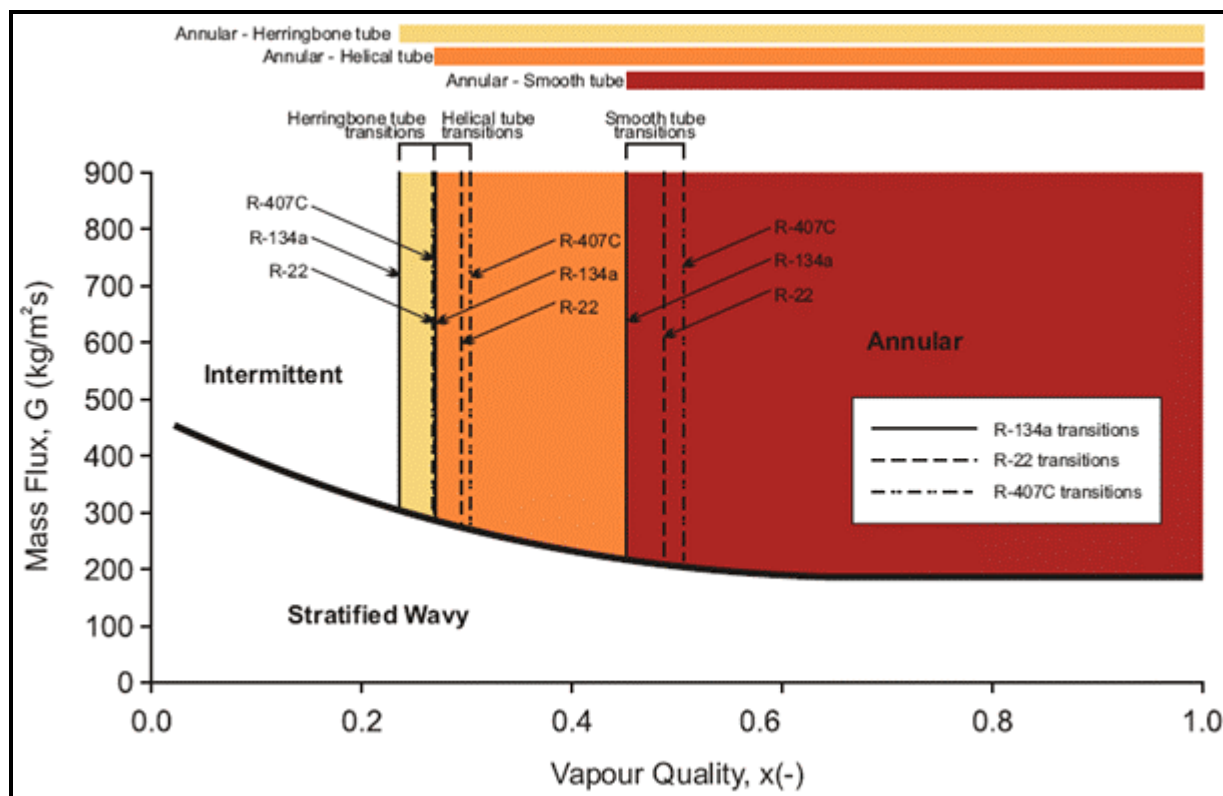


Figure 12.22. Flow pattern map of Kattan, Thome and Favrat (1998a) modified by Meyer and coworkers to illustrate their new intermittent-annular flow transitions observed for a smooth tube and two microfin tubes for three refrigerants.

12.7 Flow Patterns and Map for Two-Phase Flows over Horizontal Tube Bundles

Shell-side two-phase flow patterns (crossflow over tube arrays) and flow pattern maps have received much less attention than for intube flow. Some investigations only qualitatively described the flow patterns observed, such as Leong and Cornwell (1979), Cornwell, Duffin and Schuller (1980), Diehl (1958), Diehl and Unruh (1958) and Nakajima (1978). Other studies have attempted to quantify the observations through the development of flow pattern maps, for example those of Grant and Murray (1972, 1974), Grant (1973), Grant and Chisholm (1979), Kondo and Nakajima (1980) and Chisholm (1985). Not much work has been done on two-phase flow patterns for shell-side flows since the mid-1980's.

The two-phase flow pattern in shell-side flows is important to thermal performance as it has an effect on the two-phase friction multiplier, and hence on the two-phase frictional pressure drop. The flow pattern must also have an effect on bundle boiling heat transfer coefficients and on condensation heat transfer, but no research has confirmed this relationship so far. In any case, the knowledge of flow patterns and prediction of their transitions from one to another is key to making "thought experiments" in which the

two-phase flow structure in new systems can be predicted. Such predictions are helpful in establishing what the operating characteristics of the system will be, and thus avoid potential operating problems.

Leong and Cornwell (1979) and Cornwell, Duffin and Schuller (1980) have made visual observations of two-phase flows in a kettle reboiler slice during evaporation. They reported that two main flow patterns are dominant. In the lower zone of their 241-tube inline tube bundle, the flow was predominantly bubbly. In the upper zone where the vapor quality is larger, a distinct change in the appearance of the flow occurred, where it took on a "frothy" character. This transition was estimated to occur at a void fraction of about 60%. On the other hand, for a staggered tube bundle with two-phase upflow, Nakajima (1978) observed only bubbly and slug flows for tests at very low mass velocities and low qualities. For downflow at much higher mass velocities for a staggered tube bundle, Diehl (1957) observed only annular and spray flows. Diehl and Unruh (1958) described spray flow as one with a high-entrained liquid fraction while they defined annular flow as a flow with a low entrainment. In a more comprehensive study, Grant and Chisholm (1979) studied vertical upflow and downflow over a wide range of mass velocities and qualities in a staggered tube array, observing bubbly, intermittent (slug), and spray flows. The Diehl and Diehl-Unruh annular flow observations are probably the same as the spray flow category of Grant and Chisholm.

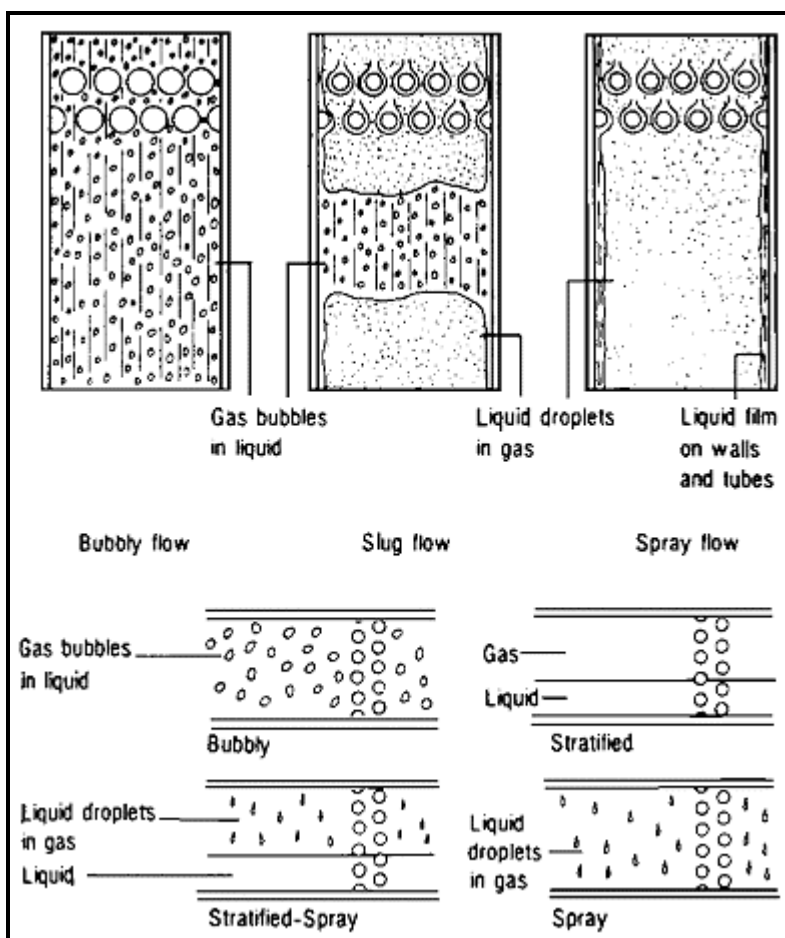


Figure 12.23. Flow patterns in tube bundles from Chisholm (1983). Upper diagram is for vertical flow and lower diagram is for horizontal flow.

For horizontal two-phase flows across tube bundles, Diehl and Unruh (1958) investigated both staggered and inline tube arrays. They observed spray, annular, slug, and stratified flows, noting that slug flow was only observed to occur in a large pitch-to-diameter ratio inline tube bundle. Grant and Chisholm (1979) and Grant (1973), on the other hand, did not observe slug flow in their horizontal flows but they did see bubbly, stratified, stratified-spray, and spray flows.

Figure 12.23 depicts and defines the names of the most prevalent flow patterns reported in the above investigations and Figure 12.24 shows the map proposed by Grant and Chisholm. Bubbly and spray flows are common to both vertical and horizontal flows while slug or intermittent flow and stratified flow generally only occur in horizontal flows. These idealized flow patterns will be affected by the leakage streams in a bundle in a heat exchanger shell, for example by flow separation around the baffles, leakage between tubes and tube holes in baffles, and any other bypass stream.

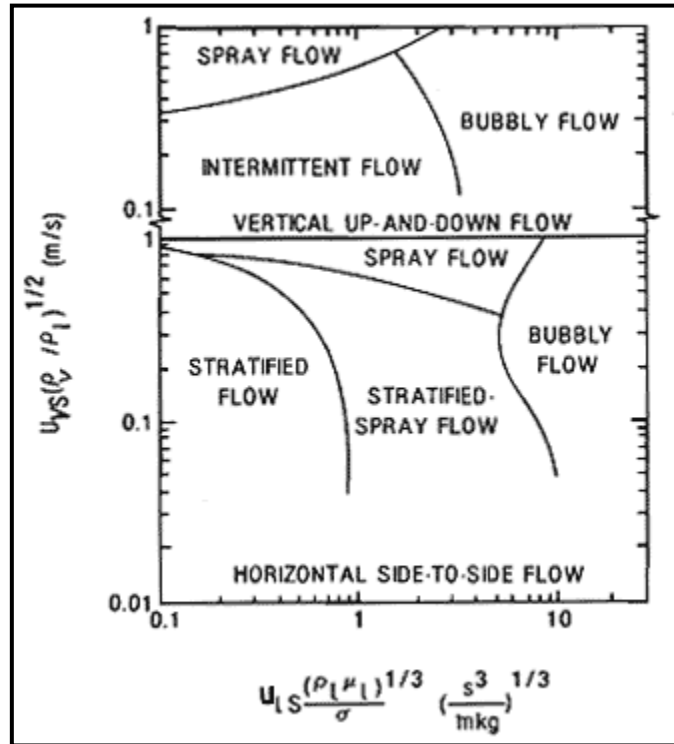


Figure 12.24. Shell-side Flow Pattern Maps of Grant and Chisholm (1979).

Chisholm (1985) more recently has presented the following transition thresholds in terms of vapor quality for horizontal flows:

$$\text{Stratified flow:} \quad \frac{1-x_S}{x_S} = \left(\frac{R-1}{B_S} \right)^{2/(2-m)} \quad [12.7.1]$$

$$\text{Bubbly flow:} \quad \frac{1-x_B}{x_B} = \left(\frac{R-1}{B_B} \right)^{2/(2-m)} \quad [12.7.2]$$

$$\text{Spray flow:} \quad \frac{1-x_F}{x_F} = \left(\frac{R-1}{B_F} \right)^{2/(2-m)} \quad [12.7.3]$$

In these equations, x_S , x_B , and x_F are the transition qualities for the stratified, bubbly, and spray transition points, respectively. The other parameters are defined as:

$$B_S = \frac{(2^{2-m} - 2)}{(Y+1)}; \quad B_B = \left(\frac{\rho_L}{\rho_G} \right)^{1/2}; \quad B_F = \left(\frac{\mu_L}{\mu_G} \right)^{m/2} \quad [12.7.4]$$

$$R = 1.3 + 0.59 Fr_L N^2 \left(\frac{\mu_L}{\mu_G} \right)^m \quad [12.7.5]$$

$$Y = \left(\frac{dp}{dz} \right)_G / \left(\frac{dp}{dz} \right)_L = \left(\frac{\rho_L}{\rho_G} \right) \left(\frac{\mu_L}{\mu_G} \right)^{-m} \quad [12.7.6]$$

and m is the exponent in a Blasius-type single-phase friction factor equation. The quantity Fr_L is the Froude number for the total flow as liquid with the velocity based on the minimum cross-sectional area in the tube bundle normal to the flow direction. The reliability of general use of these methods for prediction of flow pattern transitions is not able to be qualified here.

CONCLUSIONS

Flow patterns have an important influence on prediction of the void fraction, flow boiling and convective condensation heat transfer coefficients, and two-phase pressure drops. The prediction of flow pattern transitions and their integration into a flow pattern map for general use is thus of particular importance to the understanding of two-phase flow phenomena and design of two-phase equipment.

For vertical tubes, the flow pattern maps of Fair (1960) and Hewitt and Roberts (1969) are those most widely recommended for use. For horizontal tubes, the methods of Taitel and Dukler (1976) and Baker (1954) are widely used. The more recent flow pattern map of Kattan, Thome and Favrat (1998a) and its more subsequent improvements, which was developed specifically for small diameter tubes typical of shell-and-tube heat exchangers for both adiabatic and evaporating flows, is that recommended here for heat exchanger design. Another version of their map has also been proposed by El Hajal, Thome and Cavallini (2003) for intube condensation.

Shell side flow patterns and flow patterns maps have received very little attention compared to intube studies. Qualitative and quantitative attempts have been made to obtain flow pattern maps, but to date no method has been shown to be of general application. The flow pattern map of Grant and Chisholm (1979) has been presented here but its use must be taken as a best estimate only at this point.

Example Calculation: A two-phase fluid is flowing upwards in a vertical pipe of internal diameter of 1.0 in. The fluid properties are as follows: liquid density = 60 lb/ft³; vapor density = 2 lb/ft³; liquid viscosity = 0.4 cp; vapor viscosity = 0.01 cp. If the vapor quality is 0.2 and the total flow rate of liquid and vapor is 3600 lb/h, using the Fair flow pattern map, what is the local flow pattern expected to be?

Solution: The mass flow rate of 3600 lb/h is equivalent to 1.0 lb/s. The internal diameter is 1 in. = 1/12 ft. The mass velocity is then obtained by dividing the mass flow rate by the internal cross-sectional area of the tube, such that the mass velocity = 183.3 lb/s ft². The parameter on the x-axis of the Fair map is:

$$\left(\frac{x}{1-x} \right)^{0.9} \left(\frac{\rho_L}{\rho_G} \right)^{0.5} \left(\frac{\mu_G}{\mu_L} \right)^{0.1} = \left(\frac{0.2}{1-0.2} \right)^{0.9} \left(\frac{60}{2} \right)^{0.5} \left(\frac{0.01}{0.4} \right)^{0.1} = 1.09$$

Thus, using the values of 183.3 and 1.09 on the map, the flow regime is identified to be *annular* flow.